

Single Data Set Calibration and Imaging with Uncooperative Electromagnetic Inversion Systems

A Thesis submitted to the Faculty of Graduate Studies of The University
of Manitoba in partial fulfilment of the requirements of the degree of

MASTER OF SCIENCE

Department of Electrical and Computer Engineering University of
Manitoba Winnipeg, Manitoba, Canada

Eungjoo Kim

Copyright ©2021 by Eungjoo Kim

Abstract

After the production process, various types of grains are stored in storage facilities for years, and it is important to maintain humidity and temperature at values that ensure safe storage. Recently, Electromagnetic Imaging (EMI) systems for grain storage monitoring have been developed as an alternative method to monitor moisture content and temperature in grains while providing more sensitivity than other approaches. EMI systems use a large number of co-resident antennas usually connected to a Vector Network Analyzer via a switch. A numerical model is used to model the physical electromagnetic problem and an inversion algorithm is used to invert the collected data to produce an image of the target. However, before the computer model can be used, the raw VNA measurements must be calibrated to bridge the computational model and the true system physics. Traditional calibration approaches usually require two data sets: a data set measured from a known target for calibration purposes and a data set measured for the unknown target. We introduce and evaluate a new calibration method to calibrate and image using a single S-parameter measurement of the unknown target only. We apply this method to EMI inside of grain bins. This proposed calibration workflow: (1) estimates the bulk contents of the grain bin using a parametric inversion method and (2) uses the bulk results to subsequently estimate per-channel calibration coefficients for both the transmit and receive paths to each antenna. The novel calibration procedure is demonstrated via both synthetic and experimental results. The single-data set calibration can provide similar quality results as traditional two-data set calibration for a lab-scale experiment setup, but the technique could not produce acceptable images on the larger experiment.

Contributions

The main contribution of this thesis is to show that, in the domain of Electromagnetic Imaging, both calibration and imaging with single data set is possible. In some sense, this could be called calibration of a measurement system without reference measurements. In grain bins, like many other electromagnetic imaging systems in other application areas, it is common practise to use two (or more) sets of measurements with a known and unknown target to calibrate the system. To the authors knowledge, calibration and imaging with only a single set of measurements has not been completed previously.

This thesis is based on the work published in the following papers:

[K1] E. Kim, C. T. Mohamadi, M. Asefi, J. LoVetri, I. Jeffrey, and C. Gilmore, “Imaging and calibration of electromagnetic inversion data with a single data set,” *IEEE Open Journal of Antennas and Propagation*, 2021.

[K2] E. Kim, J. LoVetri, I. Jeffrey, and C. Gilmore, “Single data set calibration and imaging with uncooperative electromagnetic inversion systems,” in *2021 15th European Conference on Antennas and Propagation (EuCAP)*, IEEE, 2021, pp. 1–4.

Specific contributions of this author towards this work were writing MATLAB code for one-shot calibration, running contrast-source inversions, analyzing the results and writing the papers and leading the collation of the research. This author relied on co-authors to collect the experimental data.

Acknowledgements

First and foremost, I would like to thank my advisors Dr. Colin Gilmore and Dr. Ian Jeffrey for all of their support, encouragement, and guidance throughout this project. The project would not have been possible without them. Thanks also to my family, my partner Loren and my parents, for supporting me continuously and believing in me.

Contents

1	Introduction	1
1.1	Electromagnetic Imaging for Grain Monitoring	1
1.2	Traditional Calibration and Uncooperative Systems	3
1.3	Single Data Set Calibration	5
1.4	Thesis Overview	5
2	Background	6
2.1	Basic Concepts and Equations	6
2.2	Electromagnetic Wave Equation	7
2.3	The Forward Scattering Problem	9
2.4	Inverse Scattering Problem	10
2.5	Parametric Phaseless Inversion	12
2.6	Traditional Calibration	13
3	Single Data Set Calibration and Results	16
3.1	Single Data Set Calibration	16
3.1.1	Single Data Set Calibration and Generation of Scattered Fields	17
3.2	Inversion Method	18
3.3	Synthetic Results	20
3.4	Experimental Results with Small Grain Bin	23
3.5	Discussion for the Small Bin	44
3.5.1	Comparison of Computational Modelling Error in One Shot and traditional Calibration	45
3.6	Experimental Results for a Large Grain Bin	47
3.7	Discussion for the Large Bin	51

4	Conclusion	56
4.0.1	Future Research	57
5	Source Code	59
	Bibliography	69

List of Tables

3.1	Results of parametric inversion for each frequency, small bin	28
3.2	Results of parametric inversion for each frequency, large bin	49

Chapter 1

Introduction

1.1 Electromagnetic Imaging for Grain Monitoring

Various types of grain are produced all over the world and the surplus harvested grain are stored until the grain is processed, eaten, or used for next year's crop. Properly stored grain can last for years. For example, milled corn can be stored up to 112 months in dried and cooled conditions [1]. Temperature and humidity are important factors in storing grain to prevent them from deterioration [2]. Exposure to high temperatures or humidity can cause germination, mold, fungus or insect infestation in grain. Each of these spoiling mechanisms makes the grain unsuitable for consumption and destroys its economic value. In 1993, this spoilage caused by microorganisms and pest in grain and oilseeds accounts for 3 to 10% of losses in total value of unprocessed crops reported in Canada with an estimated loss of revenue of 162 to 475 million dollars per year [3].

To prevent spoilages in grain, temperature and humidity should be monitored and maintained at a low level. Conventional techniques for spoilage detection include: human observation, utilizing temperature and moisture sensors, or carbon dioxide sampling [4]. However, there are several limitations to these methods. Observation by humans, which involve an individual climbing into the bin and smelling the grain, relies on their senses which can be inaccurate, and the process of entering large grain bins to assess the grain conditions can be dangerous as air voids can form under the surface of the grain, and when an individual enters the bin these voids can suddenly collapse, trapping and suffocating the person. Temperature and moisture sensors, which are point sensors attached to a series of cables hung from the roof of the bin, tend to be costly, require

structural reinforcement to hang in the bin, and tend to become inaccurate due to dust and pollutants from the grain. These two methods as well as carbon dioxide sampling rely on a small scale sample and therefore give only a localized observation not an overall picture of a grain condition.

Electromagnetic Imaging (EMI) solves the above mentioned problems. This alternative method is capable of spoilage inspection remotely on entire bin contents with comparable installation cost [5]. Even though the exact cost is not reported, it is expected that the cost becomes more affordable when the bin is larger.

Electromagnetic imaging (EMI) is a way to create visuals of an object or space from measurements taken externally via electromagnetic waves. The technique is noninvasive and is often used to investigate a target that is not accessible. Over the past thirty years, advances in sensing technology, high-performance computers, and hardware solutions have made it possible to create more accurate images with faster processing times. These technological improvements to EMI allowed for a variety of applications in other fields of study (eg. biomedical applications [6] [7] and breast cancer detection [8,9]). EMI relies on electromagnetic fields governed by Maxwell's equations and various types of waves in the electromagnetic spectrum as a medium for interrogation. A simple imaging system is represented in Fig 1.1.

Energy is excited via a set of antennas that release electromagnetic energy as a form of wave from the transducer directing it to an object. Then, receivers around the objects measure the reflected/refracted energy. This measured energy depends on the spatial distribution of the complex permittivity, an electromagnetic property, of the the grain mass. After collecting the scattered energy, the measurements are processed using an inversion algorithm to reconstruct an image of the object which constitutes a map of

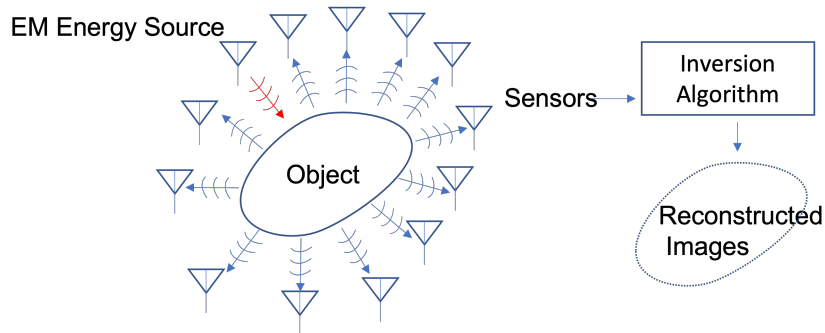


Figure 1.1: Electromagnetic Imaging Process

the complex permittivity (or complex dielectric constant). Anomalies and defects in an object can be detected as deviations from the expected permittivity of the material.

For grain storage, the temperature and moisture content should be kept low. Changes in temperature and moisture are directly related to complex permittivity. Higher temperature and moisture results in higher complex permittivity. In fact, the method of obtaining grain moisture using complex permittivity has existed for more than a century [10]. EMI uses essentially the same method, but seeks to produce a map for the entire bin rather than a small sample of the bin content.

In grain imaging, the complex dielectric can be used to indicate moisture and temperature changes [11,12]. These moisture changes represent areas of potential spoilage and are referred to as a “region of concern,” (ROC). Note that grain spoilage is a complicated process in which temperature can rise before an increase in moisture content happens as well [13], however the most relevant issue is that spoilage in grain causes both real and imaginary permittivity to be higher. The application of EMI systems related to grain imaging and spoilage detection has been previously presented in [5,14].

A grain imaging system takes measurements and then processes them to generate images. A simplified schematic of a measurement system is illustrated in Fig 1.2. The transceiver, which in practice is usually implemented as a Vector Network Analyzer (VNA) connected to a switch, generates radio frequency signals and captures the returned signal value in the form of S -parameters. The signals are exchanged via coaxial cables to RF antennas installed on the bin’s wall. Inside the bin, the signals that were generated by the VNA radiate from a single antenna while the remaining antennas receive this signal after passing through the grain. This process repeats individually for the remaining antennas to collect complete sets of S -parameters. After completing the measuring process, the collected raw measurements need to be calibrated before being input to an inversion algorithm to create a 3D images of complex permittivity.

1.2 Traditional Calibration and Uncooperative Systems

Measurements are taken and then they are sent to be processed by the inversion algorithm. The forward solver, the sources, and a mesh of the computational domain constitute the

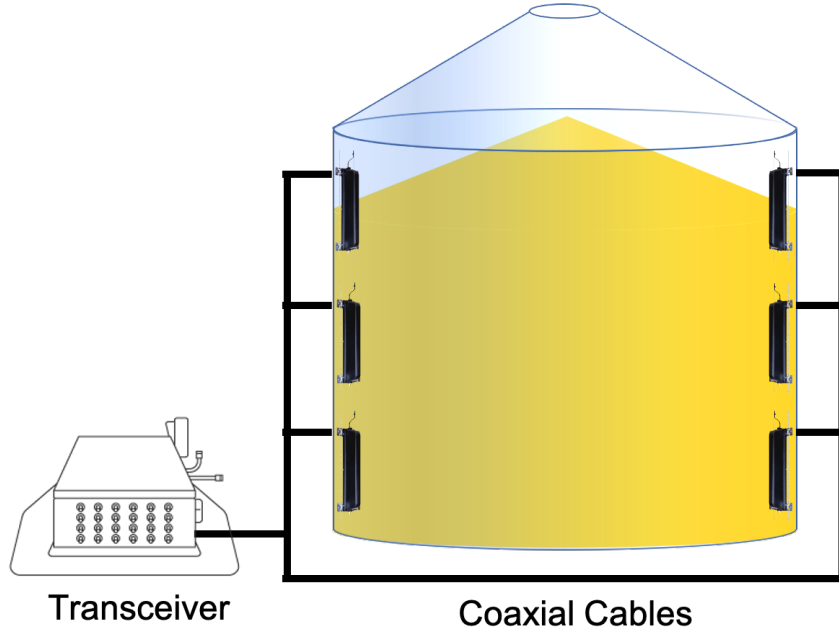


Figure 1.2: Simplified schematic of Electromagnetic Inverse Imaging (EMI) system showing only 6 antennas. 24 antennas are supported in the industrial system.

computational model of the system. Calibration for EMI is used to create a bridge between the real world and a computational model. The measurements are in a form of S-parameters, ratios of voltages, and cannot be compared directly to the output of the forward solver, which simulates electromagnetic fields. To be able to be processed by an inversion algorithm, the measurement needs to be converted to fields. This conversion, referred to as calibration, is needed for these raw measurements.

Typically, EMI system rely on differential signals to make images. That is, it takes two S-parameter measurements at two different times to form the data from which we obtain the final image. One of these two measurements is taken at a time when the target is known. In the case of grain storage, it is almost impossible to acquire this measurement because once the grain bin is filled, its contents are largely uncertain. Unfortunately, empty bin measurements aren't representative of expected imaging targets, and even if they were, removing the large volume of grain becomes impractical to capture the grain state that we want. For the purpose of this work, we will refer to these problematic systems as *uncooperative*. A new process is required to be able to work with *uncooperative* systems in practical applications.

1.3 Single Data Set Calibration

Within these uncooperative systems such as grain bins, it is not easy to measure a known system state. It would be much more beneficial if we could create images with only a single data set. In this thesis, a new calibration method is proposed that allows the scattered field to be calibrated with only a single data set. The proposed method is referred to as ‘Single Data Set Calibration’ or ‘One Shot Calibration.’ In the following chapters, a new workflow is proposed and synthetic and experimental results is shown to prove that this new calibration technique is effective.

1.4 Thesis Overview

Following the introduction, Chapter 2 explains the fundamental background information in order to understand Single Data Set Calibration: Maxwell’s equation, wave equation, forward and inverse scattering problems, Finite-Element Contrast Source Inversion, Parametric Inversion, and calibration. Chapter 3 discusses Single Data Set Calibration and its synthetic and experimental results for small and large bin is included with discussion. Chapter 4 concludes the thesis.

Chapter 2

Background

Within this chapter we introduce the concepts of a forward solver and an inversion algorithm. These two concepts are fundamental to understand the procedure of imaging and how fundamental calibration is to experimental imaging.

2.1 Basic Concepts and Equations

EMI is a modality of imaging. Imaging is a way to reproduce an aspect of an object. In imaging, we are able to recover the material parameters from the interrogation of an object. In EMI, transmitters radiate electromagnetic energy waves onto an object, and then receivers measure the resulting fields, due, in part, to the object. The fields are processed in an attempt to recover the dielectric profile of the object to recover images. These waves are governed by Maxwell's equations. Assuming an $e^{-i\omega t}$ time-harmonic convention where $i = \sqrt{-1}$, and $\omega = 2\pi f$ is the radial frequency corresponding to time-harmonic frequency f , Maxwell's equations are defined as:

$$\nabla \times H + i\omega D - J^c = J^e, \quad (2.1a)$$

$$\nabla \times E - i\omega B = -K^e, \quad (2.1b)$$

$$\nabla \cdot D = \rho, \quad (2.1c)$$

$$\nabla \cdot B = 0, \quad (2.1d)$$

where H is magnetic field strength (A/m), D is electric displacement (A · s/m²), E is

electric field strength (V/m), B is magnetic flux density ($\text{V} \cdot \text{s}/\text{m}^2$), ρ is charge density ($\text{A} \cdot \text{s}/\text{m}^3$), J^c is volume density of electric conduction currents (A/m^2), and J^e and K^e are volume density of external electric currents (A/m^2) and magnetic currents (V/m^2). Details of Maxwell's equation can be found in [15, 16]

The macroscopic Maxwell's equations are supplemented for simple linear media by the constitutive equations:

$$D = \varepsilon(r; \omega)E, \quad (2.2a)$$

$$J^c = \sigma(r; \omega)E, \quad (2.2b)$$

$$B = \mu(r; \omega)H, \quad (2.2c)$$

where ε is electric permittivity, μ is magnetic permeability, and σ is conductivity. The three constitutive parameters, which in general may represent an isotropic non-linear media, are herein assumed to be simple scalars representing linear isotropic media, an assumption that is common in most EMI applications.

The constitutive equations can be incorporated with Maxwell's equations to create field equations with isotropic material properties:

$$-\nabla \times H + (\sigma - i\omega\varepsilon)E = -J^e, \quad (2.3a)$$

$$\nabla \times E - i\omega\mu H = -K^e, \quad (2.3b)$$

2.2 Electromagnetic Wave Equation

An electromagnetic wave equation is a second-order partial differential equation that explains how electromagnetic radiation travels in a medium. It is obtained by re-writing Maxwell's equations in terms of only one of the fields, either E or H , with the benefit of making the forward solver and inversion less demanding than directly solving Maxwell's equations. In isotropic and linear materials, the inhomogenous EM equation for the electric field E can be derived using Eq. 2.3a and 2.3b.

If we assume μ is not a function of position, taking the curl of Eq. 2.3b and substituting

$\nabla \times H$ with Eq. 2.3a, we can obtain an equation:

$$\nabla \times \nabla \times E - j\omega\mu(\sigma - j\omega\varepsilon)E = -\nabla \times K^e + j\omega\mu J^e \quad (2.4)$$

For notational simplicity in introducing the concept of scattered fields below, we assume a scalar version of (2.4), the Helmholtz equation: the Eq. 2.4 can be viewed as the Helmholtz equation in a domain D_0 in frequency-dependent form:

$$\nabla^2 u(r; \omega) + \omega^2 c^{-2}(r)u(r; \omega) = -s(r; \omega), \quad (+BC) \quad r < D_0. \quad (2.5)$$

where $u(r; \omega)$ is the wavefield function, c is the speed of wave in the medium, and $s(r, \omega)$ is the source. Note that appropriate boundary conditions (BCs) are required to provide an accurate problem for these differential equations of a domain D_0 . However, specifics of BCs are inessential to understanding the concepts that are dealt with here and will not be discussed for simplicity.

While the vector wave equation 2.4 is what the numerical tools used in this work solve, for simplicity in the explanation that follows we consider the scalar version of this problem, the scalar wave equation given in 2.5.

The concept of scattered fields allows us to distinguish between the fields due to a target and those due to its surrounding medium. That is, scattered fields allow us to isolate the information that we want due to the difference between the true medium and some assumed medium.

If we define a complex wave number $k = \omega/c$ and let k_b denote the wave number of the background medium, then the total field u and incident field u^{inc} can be defined to satisfy the Helmholtz equations:

$$\nabla^2 u(r; \omega) + k^2(r)u(r; \omega) = -s(r; \omega), \quad (2.6)$$

$$\nabla^2 u^{inc}(r; \omega) + k_b^2(r)u^{inc}(r; \omega) = -s(r; \omega) \quad (2.7)$$

If we subtract Eq.2.6 and Eq.2.7, we can obtain the following equation:

$$\nabla^2 (u^{inc} - u) + k_b^2(r)u^{inc} - k^2(r)u = 0. \quad (2.8)$$

Defining the scattered field u^{sct} as the difference between the total and incident fields:

$$u(r; \omega) = u^{inc}(r; \omega) + u^{sct}(r; \omega), \quad (2.9)$$

Then from Eq. 2.9 and Eq. 2.8, we can obtain:

$$\nabla^2 u^{sct} - k^2 u^{sct} = (k^2(r) + k_b^2(r)) u^{inc} \quad (2.10)$$

By subtracting $k_b^2 u^{sct}$ right and left hand side of the Eq. 2.10, we can obtain an equation for scattered field:

$$\begin{aligned} \nabla^2 u^{sct} - k_b^2(r) u^{sct} - k^2(r) u^{sct} &= (k^2(r) - k_b^2(r)) u^{inc} - k_b^2(r) u^{sct} \\ \nabla^2 u^{sct} - k_b^2(r) u^{sct} &= k_b^2(r) \left(\frac{k^2(r) - k_b^2(r)}{k_b^2(r)} \right) u, \\ &= k_b^2(r) \chi(r) u, \\ &= k_b^2(r) w(r; \omega). \quad r \in D_0 \quad (+BC) \end{aligned} \quad (2.11)$$

The contrast χ is defined as:

$$\chi = \frac{k^2 - k_b^2}{k_b^2}, \quad (2.12)$$

contrast source w is defined as:

$$w = \chi u. \quad (2.13)$$

The contrast and contrast source are important because they are typically the functions sought when solving inverse problems in electromagnetics.

2.3 The Forward Scattering Problem

In a broader sense, the forward scattering problem refers to electromagnetic interaction problems when we know the material and cause. The forward problem is also called the direct problem. Solving a forward scattering problem means that given certain information of material and source, one is able to determine the electromagnetic field. This field can be obtained by numerically solving Eq. 2.4.

One of the basic ways to solve the forward scattering problem is to apply an integral equation method. A Green's function is used in the integral equation method and the

computational domain is limited to the domain of support of the scatterer. However, Green's functions are difficult or impossible to calculate analytically in complicated media. One way to eliminate the need for the Green's function is to use a differential-based electromagnetic solver that does not rely on an integral equation. See for example, [17].

In our research, we have used a preexisting differential based Finite-Element-Method solver, which solves Eq. 2.4 inside of arbitrary media. The Finite-Element Method, which is a type of partial differential equation (PDE), discretizes the PDE form of Maxwell's equations. In order to use FEM, the whole computational domain should be discretized and proper boundary conditions should be introduced to truncate the mesh where needed. The use of FEM is beneficial because it creates a PDE forward solver for a variety of medium boundary conditions easily. The system of equations produced is has a larger matrix size than an integral equation, but it is less dense.

The FEM solver that is used in our experiment is explained in [18].

2.4 Inverse Scattering Problem

In contrast to the forward problem where the effect is generated by the cause, an inverse problem is a process to calculate the cause when the effect is measured. Inverse problems in electromagnetics can be further specified as inverse source problems or an inverse scattering problems whether the target of interest is the source of radiation or the material of the medium. In some situations it is beneficial to first solve an inverse source problem, and to use knowledge of the source to subsequently estimate the material.

Inverse source/scattering problems are ill-posed and inverse scattering problems are also non-linear. Ill-posedness is when the problem has an infinite number of solutions and small changes in the data can cause arbitrarily large changes in the solution. Therefore, it is difficult to solve.

The Helmholtz equation in a domain D_0 is illustrated as an inverse problem in Fig. 2.1. When boundary conditions are met, the quantities (wavefield u , wave speed c , and the source s) satisfy (2.5). If any of the two quantities are known for all space, we can easily calculate the other using the equation. However, the problem is that it is impossible to know the quantities inside the target region. An inverse source problem is to determine the source $s(r; \omega)$ when u and c are known, and an inverse scattering

problem is to determine the wave speed $c(r)$ when s and u are known.

One way of solving inverse scattering problem is to solve the inverse scattering problem directly. Another way of solving is firstly to solve for the inverse source problem, and then solve for the scattering problem. As you can see from Eq. 2.11, the inverse source problem is a linear problem solving for one unknown, w , whereas for the inverse scattering problem there are two unknowns, χ and u , which is why some inversion algorithms consider the inverse source formulation [18].

In general, most inverse problems that are of practical interest are scattering problems. For example, locating oil deposits by imaging seismic structures of a region or imaging the inner body with CT scans are both inverse scattering problems used for the reconstruction of material. The grain bin imaging system is an inverse scattering problem as well. The wave speed, c of grain is reconstructed with the knowledge of an EM source and field measurements taken from a grain imaging system. The wave speed is defined as $c = \frac{1}{\sqrt{\mu\varepsilon}}$. The grain is non-magnetic, therefore the wave speed is related to permittivity ε .

There have been numerous techniques developed to solve inverse scattering problems. The contrast source inversion (CSI) is one of the ways to try to ascertain complete knowledge of the target.

CSI was first introduced for nonlinear tomography in 1997 [19], and due to its outstanding performance, the algorithm has been applied successfully to variety of applications in EMI [20–22] and biomedical engineering [17, 23, 24].

The CSI cost functional is formulated as an equation coupling the error in the data (data error) and the error in consistence between contrast source, fields, and contrast (domain error) as:

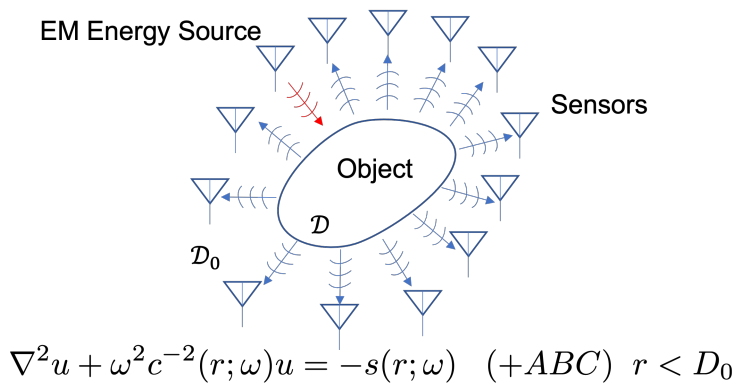


Figure 2.1: General inverse problem in a domain D_0 .

$$F^{csi}(\chi, w) = \frac{\sum_j \|f_j - \mathcal{M}_S \mathcal{L}[w_j]\|_S^2}{\sum_j \|f_j\|_S^2} + \frac{\sum_j \|\chi_j u_j^{inc} - w_j - \chi_j \mathcal{M}_D \mathcal{L}[w_j]\|_D^2}{\sum_j \|\chi_j u_j^{inc}\|_D^2}. \quad (2.14)$$

here, f_j is the scattered data that is measured at a receiver, \mathcal{L} is the forward operator that maps contrast sources to fields, \mathcal{M}_S is an operator that extracts field values at receiver points, and \mathcal{M}_D is an operator selects value within the imaging domain D . The objective function is minimized for the contrast source and the contrast iteratively using a conjugate gradient algorithm, Polak-Riebere search direction. As we use a preexisting FEM-CSI solver, the derivation, and the detailed process of discretization and optimization are excluded. For a further in-depth explanation of a FEM-CSI algorithm, see [18].

2.5 Parametric Phaseless Inversion

While FEM-CSI is an algorithm with great flexibility, the inverse scattering problem is extremely difficult because of its non-linear and ill-posed nature. Before a so-called ‘full’ inversion on each discretized piece of the grain bin is completed via FEM-CSI, we must provide FEM-CSI with a reasonable estimate of the grain height, cone angle, and average permittivity; we denote the collection of these parameters as \underline{p} . To this end, a parametric inversion algorithm is applied to the grain imaging system to extract the parameters \underline{p} . Parametric inversion is so-named because it recovers a limited number of parameters of the target (basic shape and constant permittivity of the grain) [25].

The parametric inversion serves as two purposes. First, the parameters are used as simple diagnostic information. For example, how the grain is stored in the bin and an estimate of the moisture content of the grain. Second, the parameters are used to create a background model to fully invert the data which allows one to extract more information about the target. By providing the wavenumber of the background model in the Eq. 2.12, the contrast χ is reduced. This can help reducing the non-linear nature of the problem since smaller contrast are easier to reconstruct.

However, there is still a difficulty in adopting parametric inversion on its own. As we will discuss in the next chapter, calibration is required to remove any negative effects in cables and the vector network analyzer (VNA) which is very challenging. One method to try without calibration is to try phaseless data, where only the magnitude of the signals

are used as most of the errors introduced by the measurement system affect the phase of the measured signals.

Using phaseless (magnitude only) data makes the inversion problem more ill-posed and non-linear [26, 27]. However, the corrupted phase information occurring in the physical measurements (i.e. from cables and the switching matrix) needs to be excluded to obtain more accurate results. However, since the parametric inversion only searches for a small number of parameters, this increase in non-linearity and ill-posedness is not a problem for the parametric inversion.

More details of parametric inversion can be found in [25]

2.6 Traditional Calibration

From an algorithmic perspective (i.e. once we have the data, which is assumed to be measurements of fields at a point due to a known point source), everything that we need for imaging has been discussed. However, there are still aspects that cause inversion to be imperfect. Specifically:

1. the inversion algorithm utilizes electromagnetic fields at a point, not S -parameters,
2. the difference between the physical system and the computational model requires compensation.

In phaseless parametric inversion, calibration is done in an unconventional way by using a ratio of the average values of the measurements and simulated fields for each transmitter [25]. However in general, there are two types of calibration depending on how the calibration coefficient can be obtained: incident field or scattered field calibration [28]. When the S -parameters that are collected from all receivers x and transceivers y are denoted as S_{xy} , the incident field calibration calculates calibration coefficients from the division of S -parameter of incident field S_{xy}^{inc} to modeled incident field H_{xy}^{inc} . The calibrated scattered field of incident field calibration $H_{xy,cal-inc}^{sct}$ is obtained as:

$$H_{xy,cal-inc}^{sct} = \left(\frac{H_{xy}^{inc}}{S_{xy}^{inc}} \right) (S_{xy}^{tot} - S_{xy}^{inc}), \quad (2.15)$$

where S_{xy}^{tot} are the S -parameters corresponding to the total field (true target) measurement. The total field can also be used in the calibration coefficient (H^{tot}/S^{tot}) in which

case we refer to the calibration as total field calibration; we don't consider total field calibration in this work. The scattered field calibration coefficients are obtained using the total field S^{totCal} that is obtained from the reference object installed inside imaging domain. The calibration scattered field using scattered field calibration $H_{cal-sct}^{sct}$ is obtained as:

$$H_{xy,cal-sct}^{sct} = \left(\frac{H_{xy}^{tot} - H_{xy}^{inc}}{S_{xy}^{totCal} - S_{xy}^{inc}} \right) (S_{xy}^{tot} - S_{xy}^{inc}), \quad (2.16)$$

where H^{tot} and H^{inc} are the total and incident fields of the model. The scattering field calibration requires a reference object. Since we do not have a reference object to calibrate to, we adopt incident field calibration in our work.

The process of traditional incident-field calibration used in grain bin imaging is explained in [5] and is outlined in Fig. 2.2. Under this process, the scattered field data that is used to create images using inverse imaging techniques requires two S-parameter measurements. First, measurements are taken at time t_1 when the state inside the imaging chamber is known. The state is referred to as the "known state" and the measurements are denoted as S_{xy}^{known} which plays the role of S_{xy}^{inc} . Another set of measurements are taken at time t_2 when changes might be observed in the imaging chamber, for example, after a possible ROC begins to form in the bin. This measurement is $S_{xy}^{unknown}$ which plays the role of S_{xy}^{tot} . Estimated magnetic fields of the chamber at t_1 can be obtained using the computational model in the system, as the state of the system is (assumed) known. In the grain imaging systems adopted in this work, the antennas measure tangential magnetic fields, referred to as H , on the bin wall [29]. These fields are denoted as H_{xy}^{known} . The computed magnetic fields including two measurements are used to obtain calibrated scattered fields H_{xy}^{sct} with the equation:

$$H_{xy}^{sct,cal} = \left(\frac{H_{xy}^{known}}{S_{xy}^{known}} \right) (S_{xy}^{unknown} - S_{xy}^{known}). \quad (2.17)$$

Equation 2.17 calculates a calibrated field by scaling the scattered S parameters, $(S^{unknown} - S^{known})$, by a calibration factor that aligns the model fields and measured S parameters of a known target. Traditional calibration effectively removes errors of the measurement system and attempts to convert S-parameters to fields [8,30–32]. Significant experience with calibrating many different EMI systems has shown that the known state

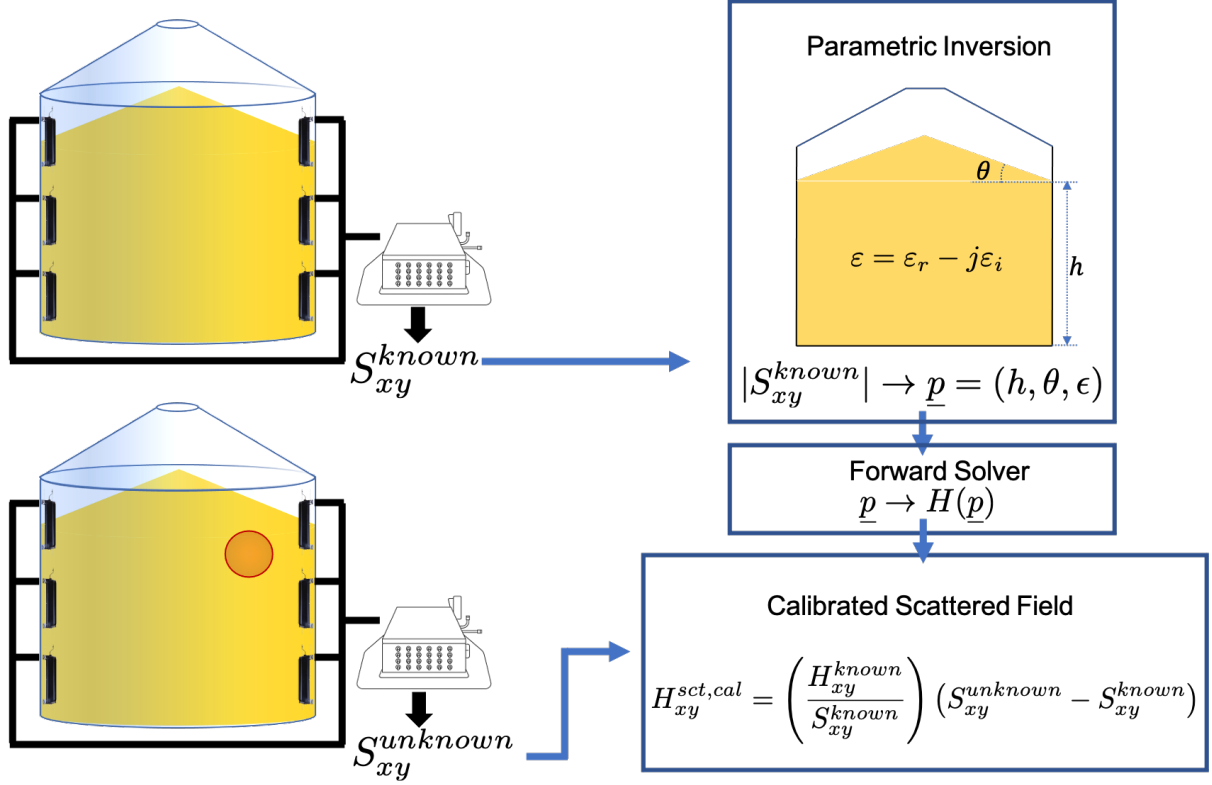


Figure 2.2: Our traditional calibration procedure reconstructs a parametric homogeneous model of a known configuration (top). The fields from the parametric model are given to a calculation where subsequent measurements are calibrated (bottom).

has to be similar to the unknown state. In particular we have found that for grain bin EMI, the bulk grain state (i.e. height/cone angle) must be the same between the known and unknown states. This is likely due to the fact that the antennas have drastically different antenna factors (which can be considered as part of the conversion of S-parameter to fields) when in or out of grain. That is, because the antennas in the grain act much differently than when they are in the air, using an empty bin as a known state doesn't work for bins with significant grain levels. In addition, traditional calibration uses one calibration coefficient for each transmit-receive pair. However, this way leads to too much flexibility in traditional calibration which makes the data over calibrated. We could expect more accurate results if the coefficients are created separately for each of the transmitters and receivers. Furthermore, it is also important to note that EMI systems with traditional calibration use differential signals ($S^{known} - S^{unknown}$) to create images. Finding a known target in an industrial imaging systems in order to get S^{known} can be a challenging task. Because of these issues with traditional calibration, we develop a new calibration technique that can compensate for these issues in the next chapter.

Chapter 3

Single Data Set Calibration and Results

In this chapter, the concept of single data set calibration and its workflow are covered. Furthermore, the synthetic results and both cases of the experimental results for both the small and large bin are provided. This chapter includes content from our published article [33].

3.1 Single Data Set Calibration

Herein, we propose a method to calibrate with a single set of S_{xy} measurements. We called this procedure ‘single data set’ or ‘single-shot’ calibration [34]¹. After the calibration process, a full 3D inversion is run on the calibrated data; the work-flow is outlined in Fig. 3.1, and consists of 4 steps:

1. Same as the traditional process, collect a single set of S -parameter data, but this time we refer to it as $S_{xy}^{unknown}$.
2. Run the parametric inversion algorithm on this data set and run a forward solver on the parameters, thus generating the total field at the receiving points produced by parametric inversion, $H(\underline{p})$
3. Perform a non-linear optimization to obtain per-channel calibration coefficients (see below for full description).

¹The core idea of this algorithm was previously presented in [34], but only for a single set of coefficients on simulated data.

4. Using the per-channel calibration coefficients, calibrate the data and send these scattered field data to the full 3D inversion algorithm.

This process allows one to generate the parametric model, calibrate, and perform a full inversion on a single data set, and is described in more detail below.

3.1.1 Single Data Set Calibration and Generation of Scattered Fields

Our proposed single-shot calibration uses $S_{xy}^{unknown}$ and H_{xy}^{known} data to obtain a set of restricted calibration coefficients (step 3 above). The key to this step of our proposed method is that we have only one calibration coefficient per transmit or receive channel (for a total of 48 coefficients in our case). Per-channel coefficients are motivated by the assumption that each transmit/receive channel can be treated as a linear system that modifies the transmitted signal only by modifying the magnitude and phase of the signal (and is independent for every channel). We use a different set of coefficients for transmit and receive mode because signals pass through different paths within the switch depending on whether the switch is in transmit or receive mode (put another way, the switch is not a reciprocal network). We represent these per-channel calibration coefficients as diagonal matrices:

$$C_x = \begin{bmatrix} c_{x1} & & \\ & \ddots & \\ & & c_{xN} \end{bmatrix}, C_y = \begin{bmatrix} c_{y1} & & \\ & \ddots & \\ & & c_{yN} \end{bmatrix}, \quad (3.1)$$

where N is the total number of antennas (i.e. transmit/receive channels) and c_{xj} is the complex calibration coefficient for receive path j , $j = 1, 2, \dots, N$, and c_{yj} is the transmit path. These are used to capture the phase shift and channel loss of the signal pathway.

We obtain estimates of these calibration coefficients, $C = [C_x, C_y]$, by minimizing the following objective function:

$$C = \underset{\tilde{C}}{\operatorname{argmin}} \quad ||\tilde{C}_x S^{unknown} \tilde{C}_y - H(\underline{p})||_2^2, \quad (3.2)$$

where $S^{unknown}$ are the raw measurements, and $H(\underline{p})$ are the total fields at the receive points obtained from the parametric inversion (step 1). The C matrices are diagonal, and e.g. the result of $c_{x2} S_{2,1} c_{y1}$ thus represents the calibrated field from receive channel

2 and transmit channel 1.

Based on the diagonal structure of the C matrices we have $(CS^{unknown}C)_{xy} = c_x S_{xy}^{unknown} c_y$ which clearly shows that the coefficients c_x and c_y act to account for cable loss and phase shifts along the channels x and y in the measurement path that are not accounted for in the forward model used to generate $H(\underline{p})$.

The justification of our per-channel calibration model is that the main component of the signal deterioration is simply a magnitude and phase shift in each transmit/receive channel in the measurement system. A full calibration would require a calibration matrix the same size as the S matrix, rather than a diagonal matrix. Our use of diagonal C matrices means that cross-channel signal leakage is currently being ignored in our proposed calibration method. However, the problem of this leakage is minimized by design in the switch where the majority of leakage occurs. Another way of viewing our use of diagonal calibration matrices is that each channel is considered to be a lossy transmission line (not a full-port device between the VNA and the antennas). The coefficient C -matrix also accounts for the antenna factor (that compensates for the change between the field and voltage ratio measurements).

Once matrices of per-channel calibration coefficients for both signal paths are determined by optimizing 3.2, the calibrated scattered field data $H_{xy}^{sct,cal}$ are calculated as:

$$H_{xy}^{sct,cal} = C_x S^{unknown} C_y - H(\underline{p}). \quad (3.3)$$

That is, the bulk parametric inversion p serves not only to provide an approximate known state for calibration via 3.2, but also serves as the background medium used to define the scattered fields for subsequent inversion. The calibrated scattered fields, $H_{xy}^{sct,cal}$ can now be sent to the inversion algorithm.

3.2 Inversion Method

Once $H^{sct,cal}$ is produced by the single-shot calibration process, we can proceed to apply an inversion algorithm to detect ROCs that may be present in the grain. This is accomplished using a parallel 3D Finite-Element Contrast Source Inversion Method (FEM-CSI) algorithm. Details of the basic FEM-CSI algorithm are discussed in chapter 2.5, and its application to the grain bin problem is presented in [5, 14, 35].

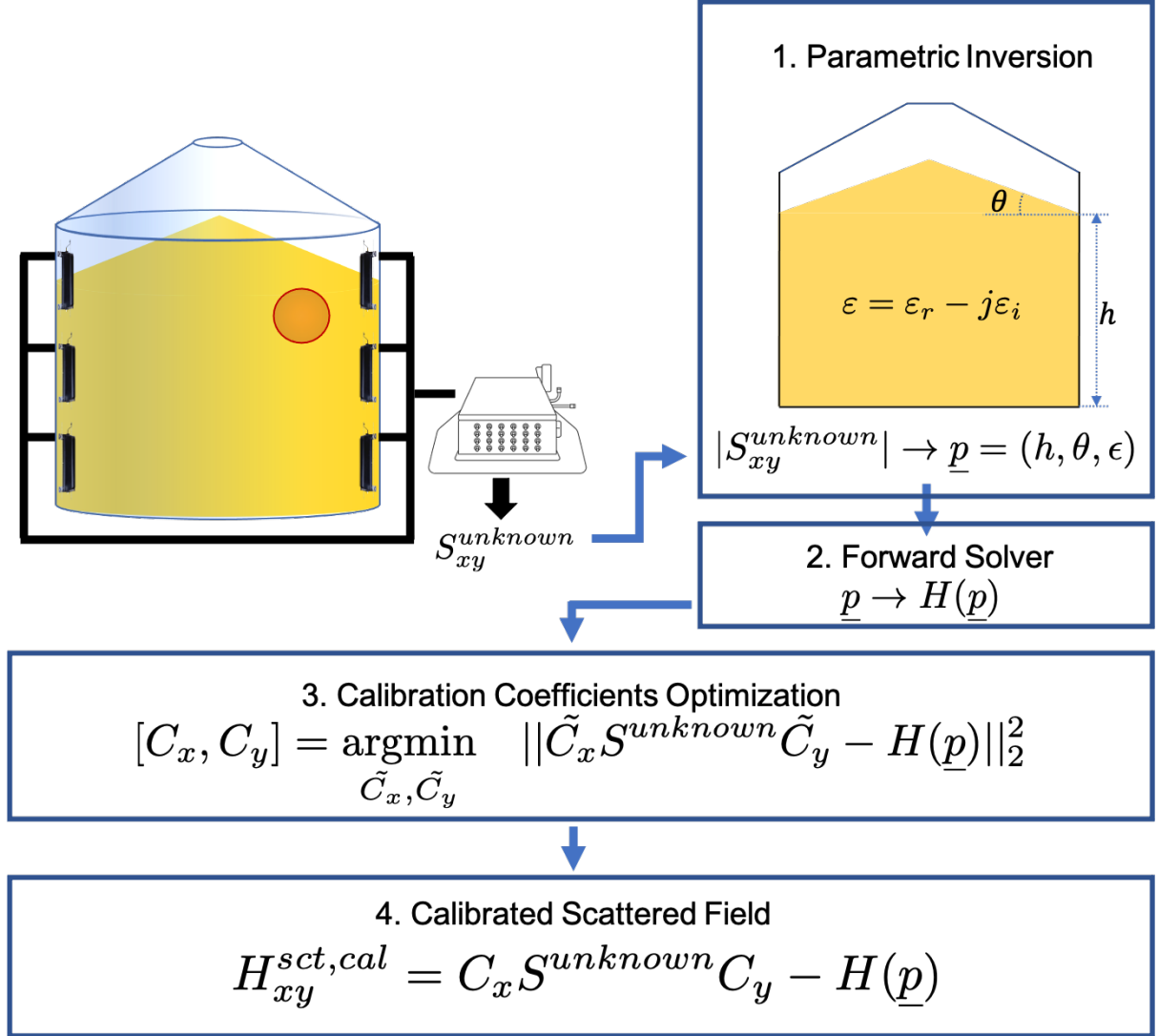


Figure 3.1: The proposed single-shot calibration method consists of 4 steps: 1) phaseless parametric inversion optimizes on parameter \underline{p} with a single S -parameter measurement, 2) a forward model is created with \underline{p} , 3) channel-specific calibration coefficients are determined through optimization, and 4) the parametric model and calibration coefficients are used to produce calibrated scattered-fields.

3.3 Synthetic Results

To show the effectiveness of the proposed single-shot calibration method, we first consider a synthetic analysis with bin dimensions and frequencies chosen to mimic an experimental system. The bin features a flat-bottomed bin with a wall height of 25.75 m and a diameter of 23.64 m. Twenty four (24) antennas are installed on the interior of the bin wall, placed at 12 different radial locations in pairs (similar to the hour indicators marked on a clock). Antenna heights are selected to maximize the number of possible antennas heights given the restrictions of bin construction (i.e., antennas must avoid the bolts that hold the bin together). A simple schematic of the synthetic bin is illustrated in Fig. 3.2. A frequency of 17 MHz was selected for this experiment (a wavelength of 17.6 m in free space). The parameters of the simple grain model are given as $h = -4.0$ m, $\theta = 15^\circ$, and $\varepsilon_{rel} = 4.1 - j0.48$. A spherical ROC is submerged in the grain. The ROC's permittivity is $7 - j0.8$ and its diameter is 3 m (or $\approx 1/6$ of a wavelength in free space). The total fields H^{tot} of this synthetic configuration were then generated with a full-3D FEM based forward direct solver [18].

Next, simulated per-channel shifts were added through per-channel magnitude and phase shifts to create synthetic measurement system errors: $S^{unknown} = (C_x^{synth})^{-1} H^{tot} (C_y^{synth})^{-1}$, where C_x^{synth} and C_y^{synth} were created based on estimates of cable phase shifts and losses from the experimental system installed on the bin on which this synthetic experiment was modelled. These data, $S^{unknown}$, provide the initial input to our proposed single-shot calibration method. The magnitude and phase of the true transmit/receive coefficients C_x^{synth} and C_y^{synth} are shown in Fig. 3.3.

Step 1 of the proposed method is to obtain the material parameters \underline{p} of the estimated background model via phaseless parametric inversion. We note that the ROC cannot be represented by the parametric model as the permittivity of this model is expected to be homogeneous, but the fields caused from the ROC are present in the simulated S-parameter measurements. The inverted parameters were obtained as $\varepsilon_{rel} = 4.09 - j0.47$, $h = -3.89$ m and $\theta = 12.31^\circ$ and matched well when compared to the true values. $H(\underline{p})$ was generated using these parameters.

Moving on to Step 2 of the proposed calibration scheme we next solved (3.2), using the non-linear optimization tool provided in Matlab. This procedure produces estimates of the Tx/Rx coefficients of C_x^{synth} and C_y^{synth} . The estimated coefficients C after the

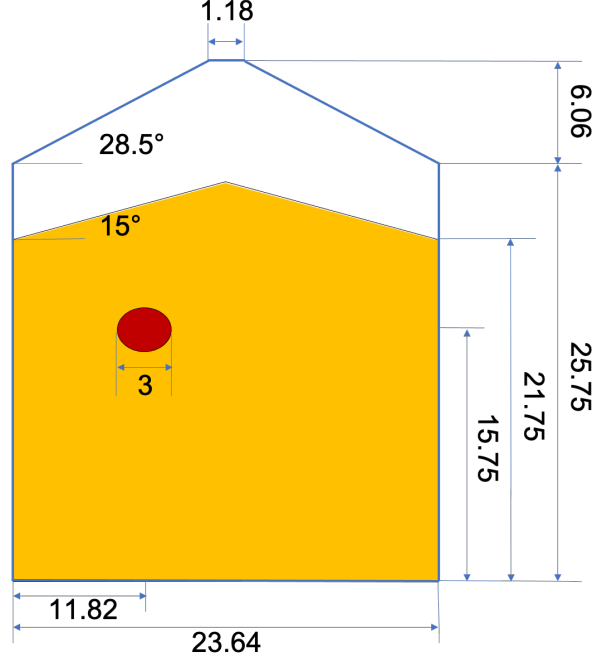


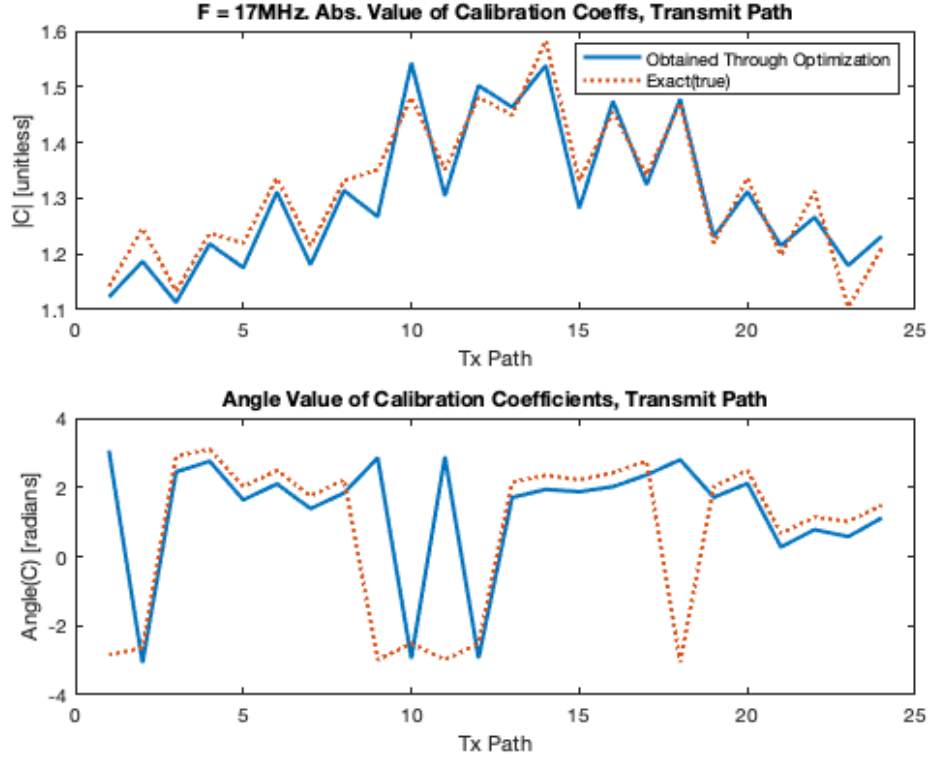
Figure 3.2: Layout of flat-bottom style grain bin for synthetic test. The permittivity of the grain is $4.1 - j0.48$ while the permittivity of the ROC is $7 - j0.8$.

optimization are shown in Fig. 3.3. These optimization-generated coefficients are quite close to the true values, but not exact. The complex percent relative L_2 -norm of the true vs estimated are 15.2% for the transmit path and 19.0% for the receive path coefficients. We do not expect exact values between the true C 's and recovered C 's as the fields from the ROC and errors in the phaseless parametric optimization (i.e. errors in our parameters p), mean we cannot obtain an exact fit for the C matrices. While there is clearly some error between the true and estimated C 's, the ultimate determination whether the estimated values are accurate enough is in the generation of the inverted images based on these estimated C 's. We turn to those images next.

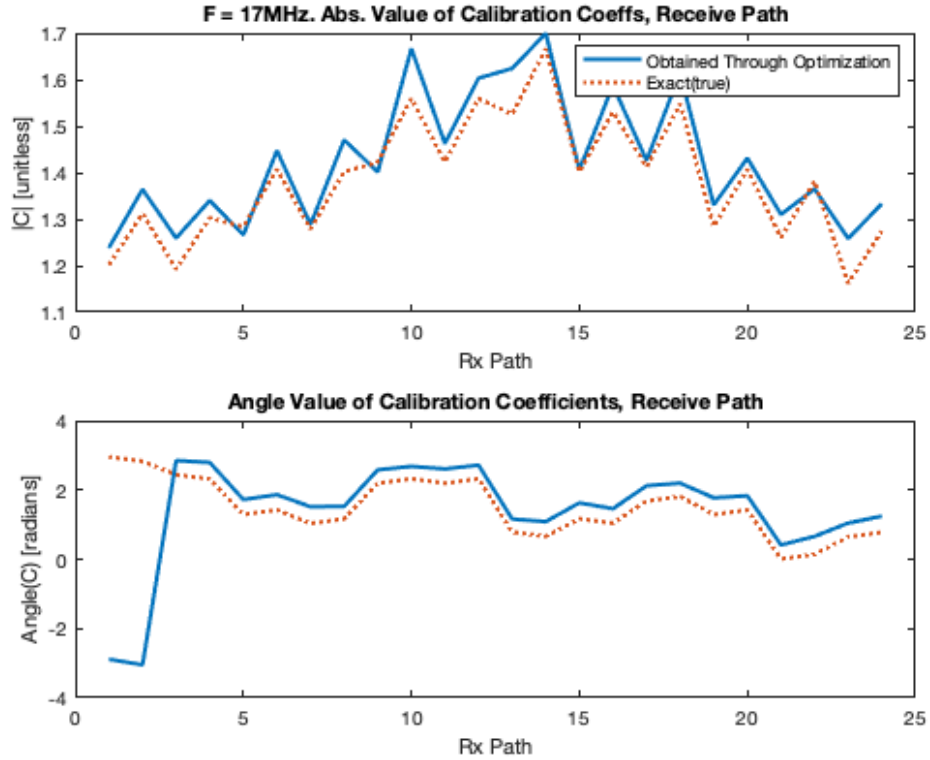
The calibrated scattered fields are obtained following (3.3) and are given to the FEM-CSI algorithm. The inversion results using the proposed single-shot calibration are shown in Fig. 3.4 (a), and Fig. 3.5 (a)-(b).

The benefit of using a synthetic example rather than experimental data is that images can also be generated for the case without cable coefficients. Specifically, we create a near 'ideal' image using the following data:

$$H^{sct,ideal} = H^{tot} - H(\underline{p}). \quad (3.4)$$



(a)



(b)

Figure 3.3: Calibration coefficients used for the synthetic analysis. (a) Calibration coefficients per transmit channel. (b) Calibration coefficients per receive channel. The exact coefficients used to manipulate the synthetic data are shown in red, the estimated coefficients computed from optimization are shown in blue.

$H^{sct,ideal}$ is the ideal scattered field data and the data do not include errors in the measurement system (but note that they still include the imperfect parametric-obtained background field as we use the same $H(p)$ for both the ‘ideal’ and one-shot case). A more accurate image could be obtained by utilizing the perfect background information (i.e. use the homogeneous grain bulk without the ROC region). However, this perfect prior information is not accessible for actual bins, so we have instead used the available parametric-generated prior information. The results of the 3D FEM-CSI inversion on these ideal data are shown in Figs. 3.4 (b) and 3.5 (c)-(d). The results obtained via the single-shot (proposed) calibration are very similar to the ideal results, demonstrating the potential of the proposed one-shot calibration method. This synthetic result shows that the recovered C’s are precise enough to generate acceptable final images, even if the parametric inversion does not provide accurate results due to the presence of the ROC.

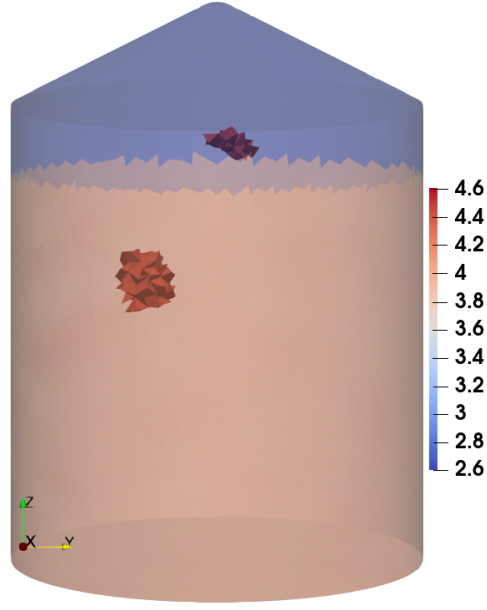
The next test discusses experimental data.

3.4 Experimental Results with Small Grain Bin

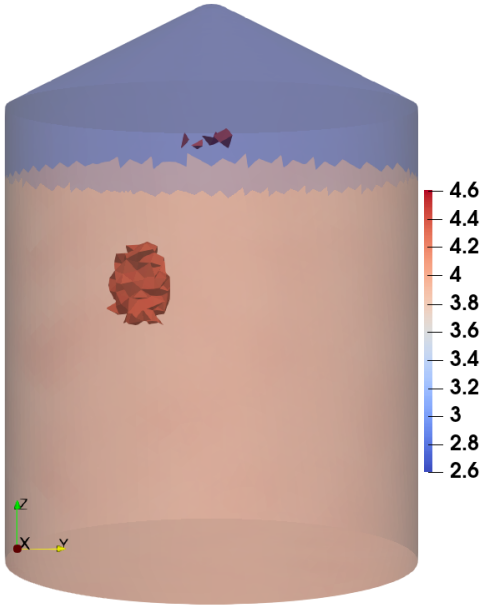
As an experimental test, we applied the one-shot calibration method to a scaled (small) grain bin that was previously reported in [29, 36]. We used the scaled bin as we can perform a controlled experiment: it is feasible to create and control the ROC in a homogeneous background of grain which is much more difficult in a larger bin. The barrel’s schematic diagram and images of the interior of the test barrel are shown in the Fig. 3.6.

The experimental bin is a cylindrical metal barrel that has a height of 0.81 m and a radius of 0.28 m. The volume of this lab-sized bin is about 190 L (4.5 bushels). 24 antennas are installed inside the grain bin wall in a stair case style in order to spread the antennas out on the bin wall as much as feasible. In order to keep air circulated throughout the grain, a false-bottom floor was welded at a height of 10 cm from the ground, and the lid was placed on top but not tightened. In contrast with previous reports with this system [36], we have added ferrite behind each antenna, which has the main effect of increasing the signal strength. These modified antennas are described in [37], but operate in a very similar manner to previously reported antennas in [36] (with an increase in signal strength).

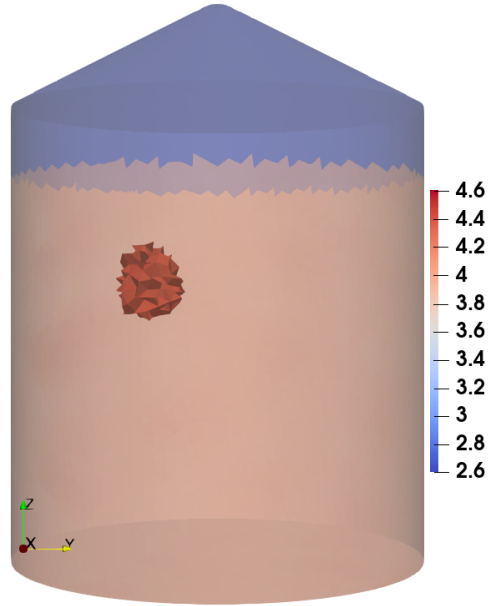
The antennas are connected to coaxial cables via a switch to transfer data to a VNA.



(a) Single-shot Calibrated Image
(synthetic data)



(b) Image with No Measurement Error (para-
metric background)



(c) Image with No Measurement Error (inci-
dent background)

Figure 3.4: FEM-CSI inversion 3D image of $\Re(\epsilon)$ with a threshold. (a) The outcome of the single-shot calibration procedure on synthetic data manipulated with per-channel magnitude and phase shift. (b) Ideal results without measurement error using the same parametric background. (c) Ideal results without measurement error using the perfect background. All tetrahedrons beyond a threshold of 4.4 are solid. The one-shot calibrated image compares favorably with the ideal image.

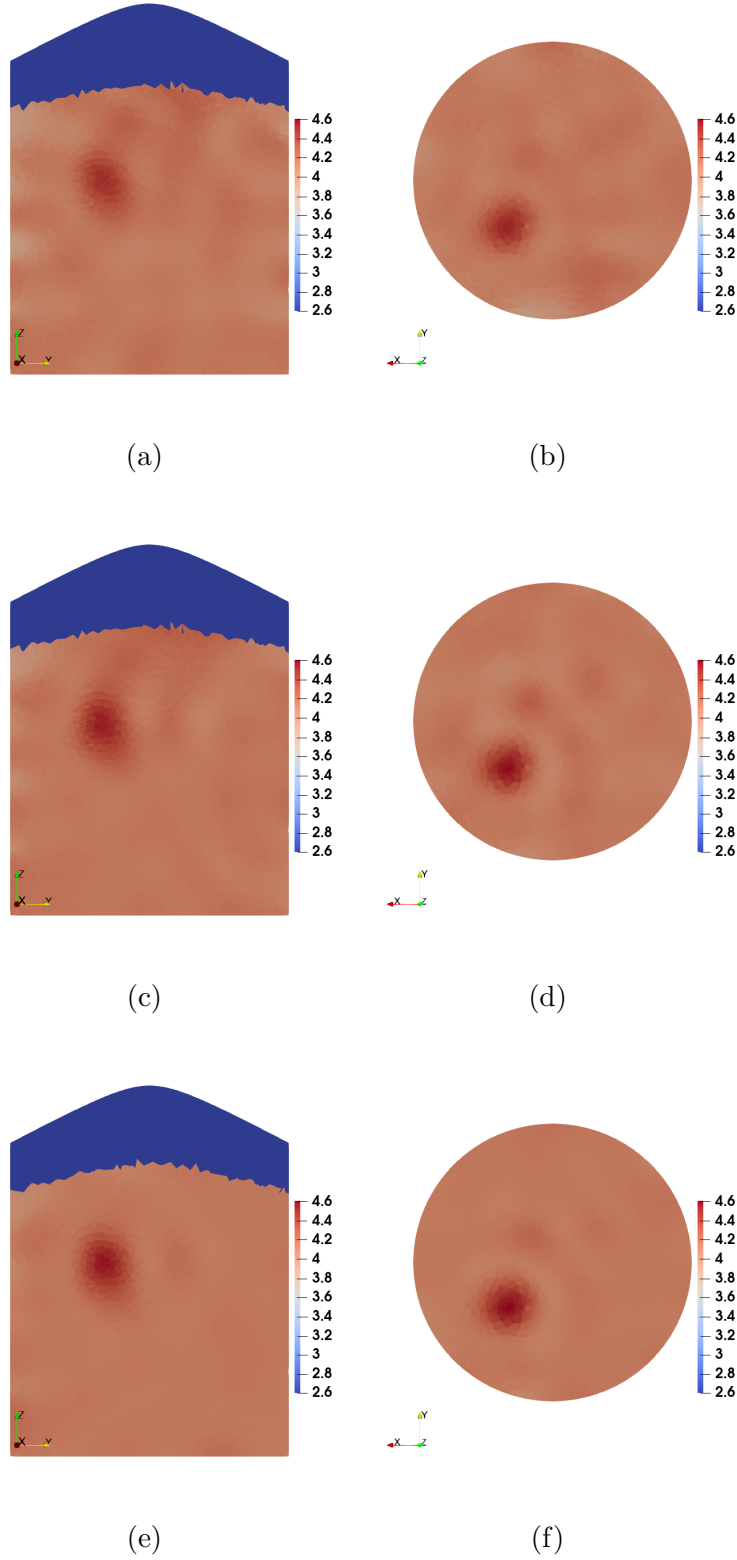


Figure 3.5: Further 2D slices of the FEM-CSI result for the synthetic single-shot calibration. (a) Vertical slice and (b) horizontal slice of the one-shot calibrated data inversion. (c) Vertical slice and (d) horizontal slice of the 'ideal' data inversion with the same parametric background. (e) Vertical slice and (f) horizontal slice of the 'ideal' data inversion with the perfect background.

S -parameter measurements are taken over a range of frequencies from 1 to 1300 MHz. In our experiment, we chose six frequencies from the 240–270 MHz and the 550–570 MHz bands (260, 270, 280, 550, 560, and 570 MHz). We chose the lower band as it is located in the resonance of the antennas [37] and the higher band was chosen to match other frequencies previously used in this scaled grain bin [36]. The wavelength of 250 MHz band is ≈ 0.70 m in grain and 550 MHz is ≈ 0.32 m in grain.

The barrel was filled with hard red spring wheat and the top surface of the grain was made flat. The grain had a moisture content of 7.5%, which literature values estimate to have a permittivity of approximately $\epsilon_r = 3 - j0.3$ at 250 MHz [38]². We then collected the first data set of the homogeneous grain: S_{xy}^{known} .

We then created a ROC (or target) by adding 210 g of water to 1410 g of grain in a double sealed plastic bag. If all the water had been absorbed, the moisture content of the grain would be 19.5 % (wet basis). If all of this water was to be absorbed by the grain, the approximate permittivity of the grain target would be $\epsilon_r = 4.5 - j0.6$ [38]³. The wet-grain target is shown in Fig. 3.6 (c), and the approximate dimensions were $8 \times 14 \times 11$ cm. With the help of a plastic pail, we excavated a void the grain and placed the high-permittivity target in the background dry grain. Finally, we filled up the remaining space in the plastic bucket with dry grain to level the grain height. This process simulates, in a controlled fashion, how grain typically spoils in bins. Finally, we measured the target data set $S_{xy}^{unknown}$.

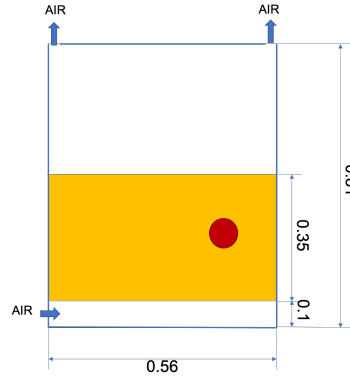
As with the synthetic example, we used the $S_{xy}^{unknown}$ measurements in the phaseless parametric inversion algorithm. Parameters after optimization are presented in Table 3.1. An average permittivity was estimated as $3.17 - j0.42$ from frequencies in the 250 MHz band, and as $2.92 - j0.35$ from frequencies in the 550 MHz band. The difference is expected because wheat permittivities are lower at higher frequencies [38]. The estimated angle and the height are consistent with the overall frequencies, and have an average of 4.17°

²We note that this value of permittivity is quite approximate. The density temperature and particular sub-type of wheat affects the exact value of the the permittivity of grain [10]. However, for our purposes the exact expected value is not needed: the bulk permittivity value is obtained from the parametric inversion step.

³Again, this is an estimate. This imaging experiment was performed approximately one hour after mixing the water into the target. Grain can only fully absorb about 2 % moisture per day, so the water was not fully absorbed at the start of the experiment, which means the precise permittivity of the target is not available. However, since the goal of this paper is to compare the traditional calibration with the proposed method, the exact permittivity of the target does not change our conclusions. The important point is that the permittivity is higher than the dry background grain.



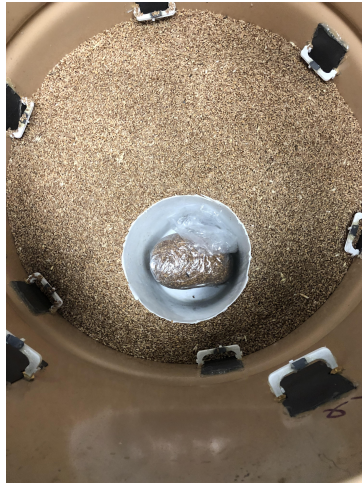
(a)



(b)



(c)



(d)



(e)

Figure 3.6: (a) Exterior photograph of the barrel with the VNA/switch connected to all 24 antennas. (b) Schematic diagram of model grain bin. (c) Image of the wet-grain target with marker for scale. Images of the interior of the barrel are shown in (d) and (e). Grain was filled with a wet grain mixture covered in plastic in a bucket. (d) Dry grain is placed in the bucket then (e) we covered up to the wet grain mixture and leveled the grain.

Table 3.1: Results of parametric inversion for each frequency, small bin

Frequency (MHz)	ε_{rel}	Est. Height (from the eave top, meters)	Est. Angle (degree)
260	3.17 - $j0.44$	-0.38	-0.11
270	3.18 - $j0.43$	-0.37	-3.43
280	3.16 - $j0.41$	-0.4	9.74
550	2.95 - $j0.34$	-0.38	0.57
560	2.93 - $j0.35$	-0.38	6.87
570	2.89 - $j0.36$	-0.38	11.4

and -0.38 m ⁴. Next, the homogeneous background model was generated using those parameters. As explained previously for the synthetic test, the ROC cannot be captured from this process.

The next step is to compute calibration coefficients using the background model $H(\underline{p})$ and raw measurement $S^{unknown}$. The calibration objective function of (3.2) is minimized to be able to capture calibration coefficients in the transmit and receive state. The coefficients that were computed from this process between transmit and receive state vary greatly. The coefficients are shown for each frequency in Fig. 3.19. As this is experimental data, we do not have access to the true values.

The next step was to compute the calibrated scattered fields and the process was finalized by sending the data to CSI-FEM inversion. Grain permittivity of $\Re(\varepsilon)$ is shown in Fig. 3.7 for 260, 270, and 280 MHz, and $\Re(\varepsilon)$ is shown in Fig. 3.13 for 550, 560, and 570 MHz. We also show 3D threshold images in Figs 3.11 and 3.17.

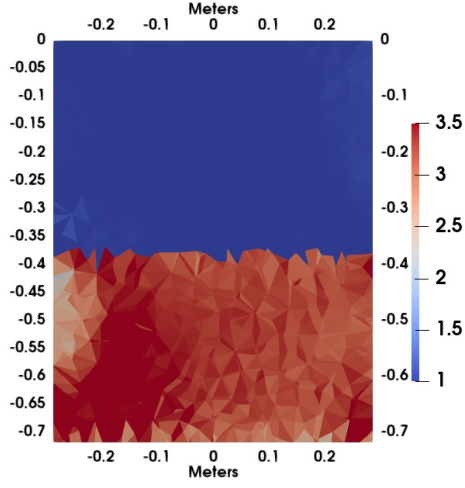
Grain permittivity of $\Im(\varepsilon)$ is shown in Fig. 3.9 for 260, 270, and 280 MHz, and $\Im(\varepsilon)$ is shown in Fig. 3.15 for 550, 560, and 570 MHz. However, we do not normally consider the imaginary component because (1) all the work on converting permittivity to moisture in the literature (and industrially) uses the real part of the permittivity as imaginary part varies significantly from variety to variety (e.g. two different varieties of wheat will have different relationships between imaginary permittivity and moisture content, and there is even large variations within the same batch wheat from the same variety [11]) and (2) we often get poorer reconstructions in the imaginary part for unknown reasons. Beyond these figures, we do not present the images of the imaginary components again (as in this

⁴There are more errors in the cone angle, which is common as the phaseless parametric inversion algorithm is not as sensitive to cone angle.

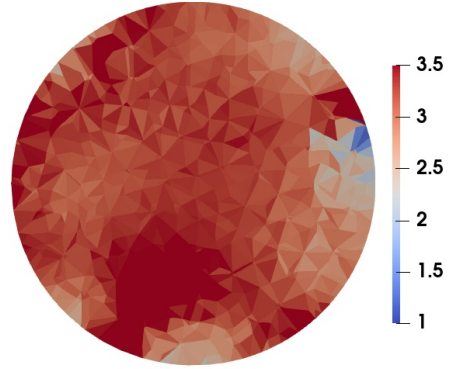
case, they do not show the target region very well).

Traditional Calibration: In order to determine the quality of the single-shot calibrated images, we compare it to a traditional calibration approach. We thus applied traditional two data set calibration by generating the parametric fields associated with S_{xy}^{known} , and followed the calibration process outlined in (2.17). Other than changing the calibrated data, we keep all other parameters (meshes and stopping condition) of the FEM-CSI inversion were identical between the single-shot and traditional methods. The images associated with traditional calibration process are shown in Figs. 3.8 and 3.14. We have also presented 3D threshold images in Figs. 3.12 and 3.18.

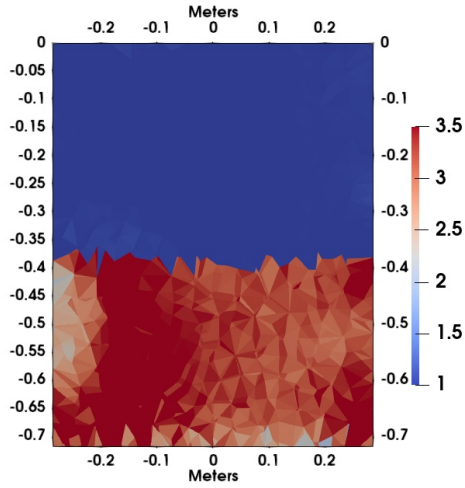
Single-shot work flow when no wet-grain target is present: As a final step for small bin experiment, we considered the case where we run the single-shot workflow on a data set collected where there is no wet-grain target present. That is, $S_{xy}^{unknown}$ contains only homogeneous grain. We perform this experiment in order to show that our detection of the ROC is not an accident. If our proposed calibration method works, then performing the test on this homogeneous example should show final results with no ROC. For a frequency of 550 MHz, these results are shown in Fig. 3.20.



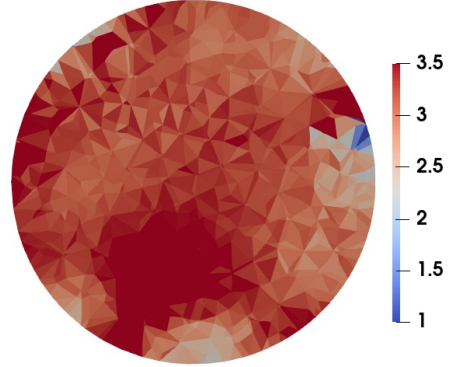
(a)



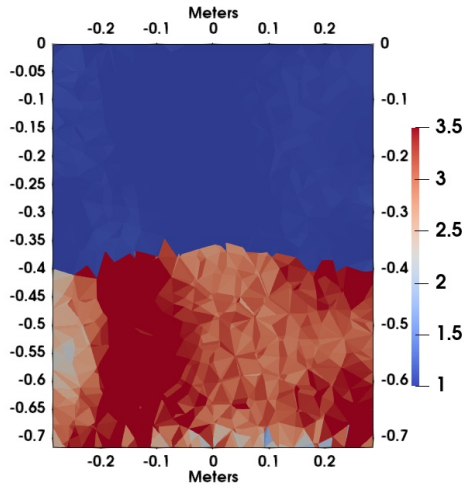
(b)



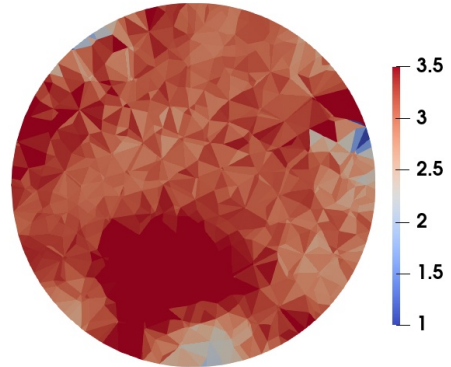
(c)



(d)

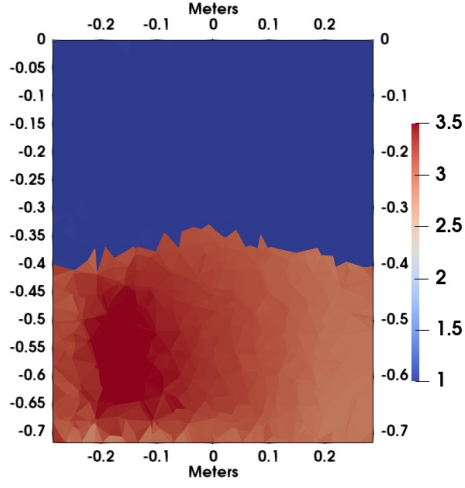


(e)

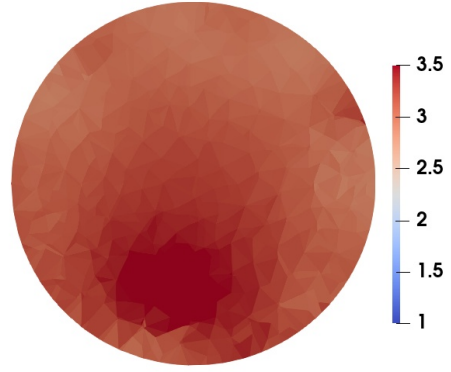


(f)

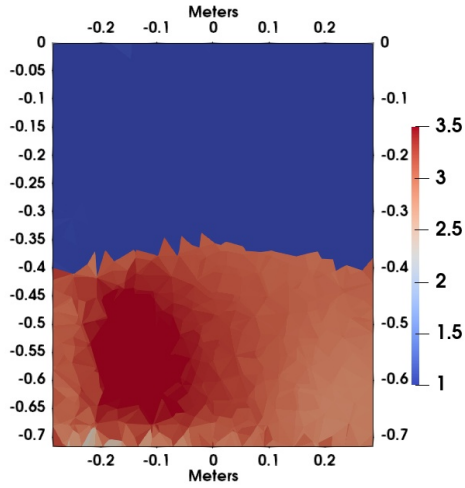
Figure 3.7: One-Shot Calibrated Experimental FEM-CSI imaging results of $Re(\epsilon)$ for the frequency band 200MHz. One-shot calibration (a) vertical and (b) horizontal slice at 260MHz, (c) vertical and (d) horizontal slice at 270MHz, and (e) vertical and (f) horizontal slice at 280MHz.



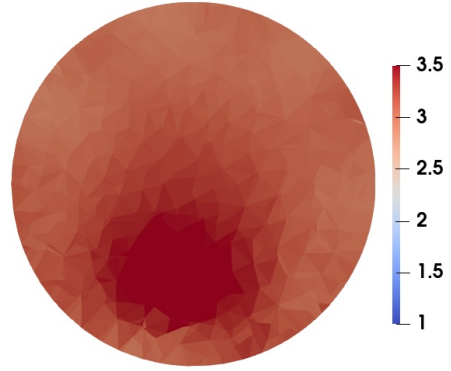
(a)



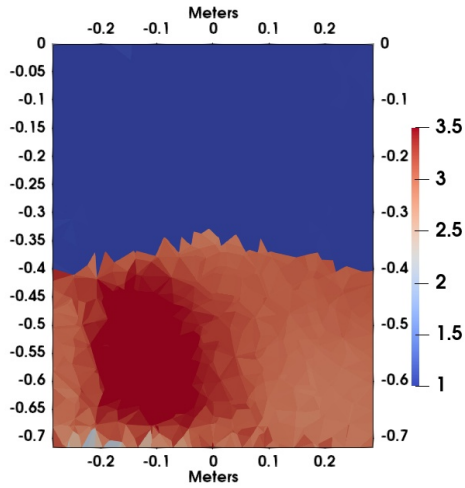
(b)



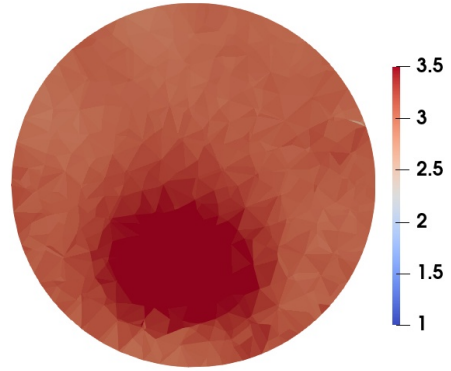
(c)



(d)

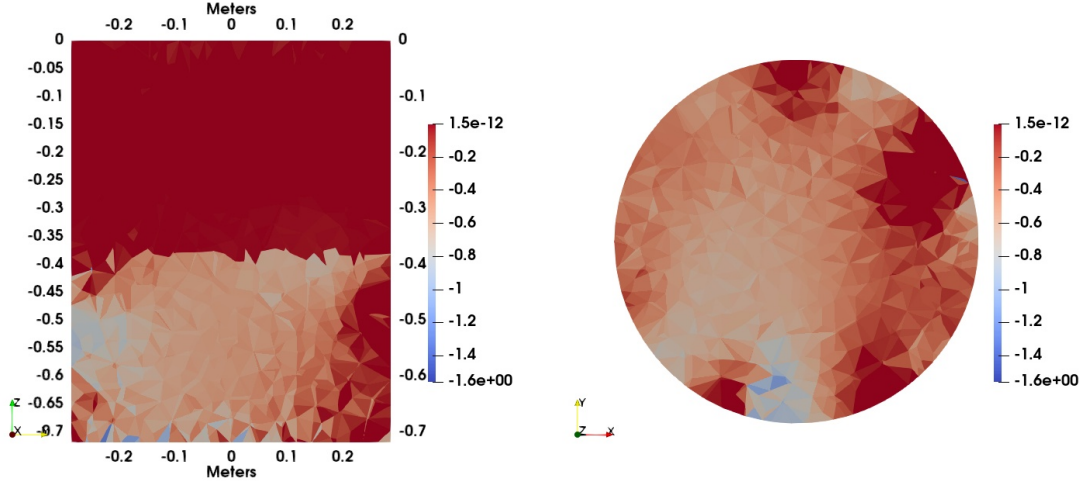


(e)



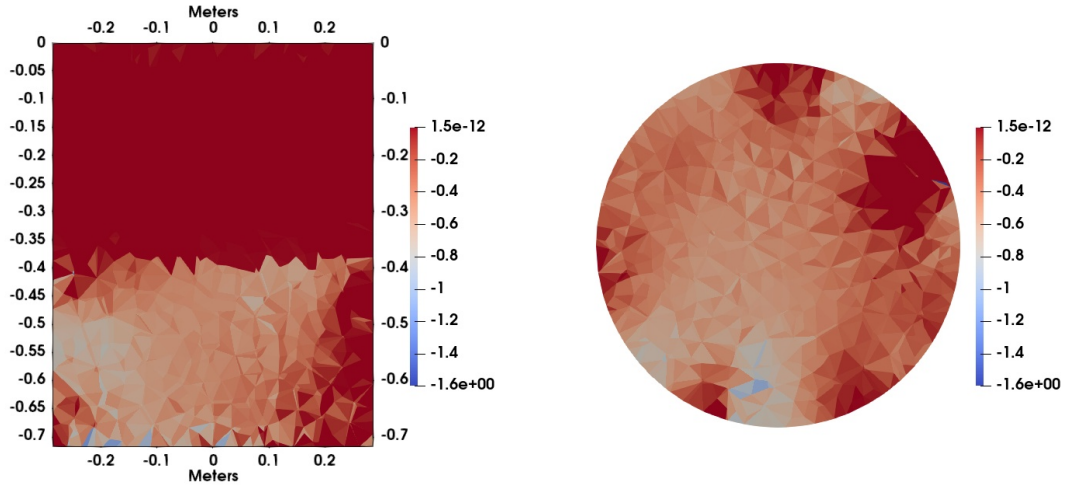
(f)

Figure 3.8: Traditional Calibrated Experimental FEM-CSI imaging results of $Re(\epsilon)$ for the frequency band 200MHz. Traditional calibration (a) vertical and (b) horizontal slice at 260MHz, (c) vertical and (d) horizontal slice at 270MHz, and (e) vertical and (f) horizontal slice at 280MHz.



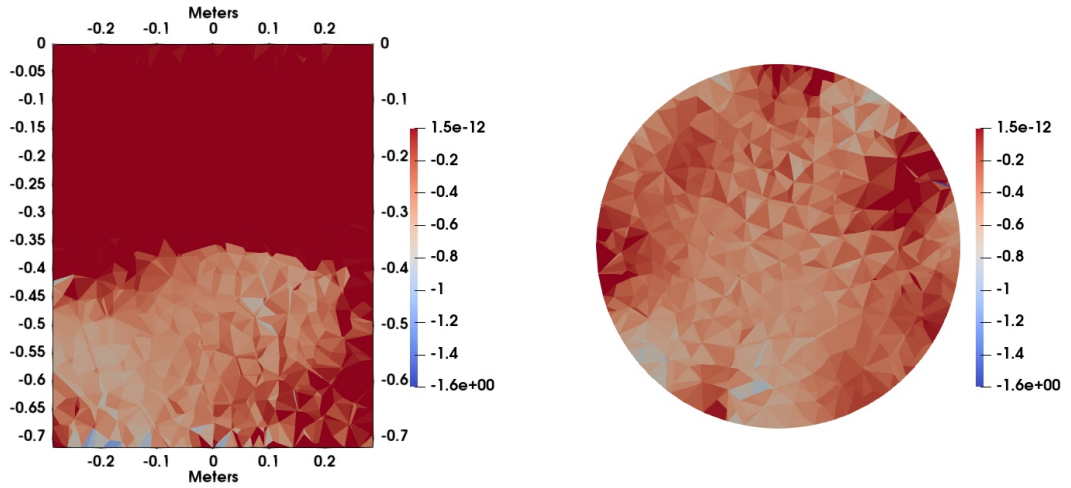
(a)

(b)



(c)

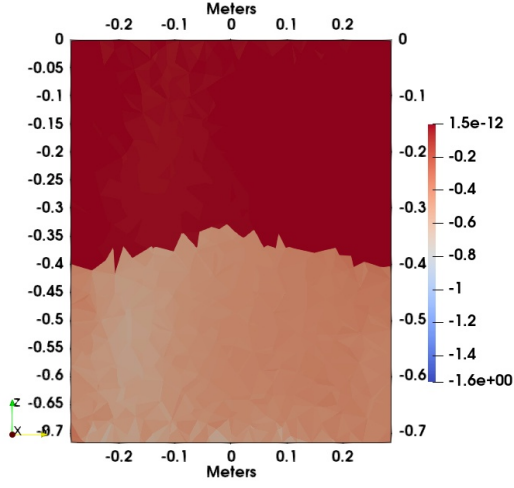
(d)



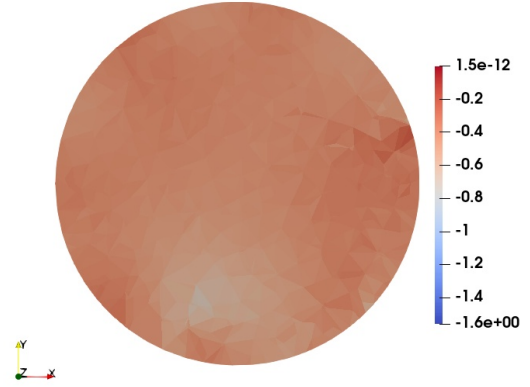
(e)

(f)

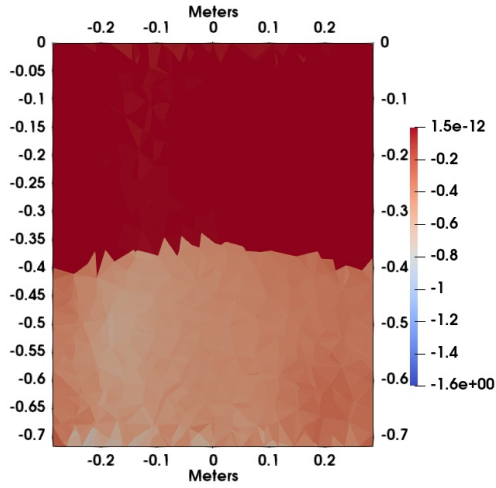
Figure 3.9: One-Shot Calibrated Experimental FEM-CSI imaging results of $Im(\epsilon)$ for the frequency band 200MHz. One-shot calibration (a) vertical and (b) horizontal slice at 260MHz, (c) vertical and (d) horizontal slice at 270MHz, and (e) vertical and (f) horizontal slice at 280MHz.



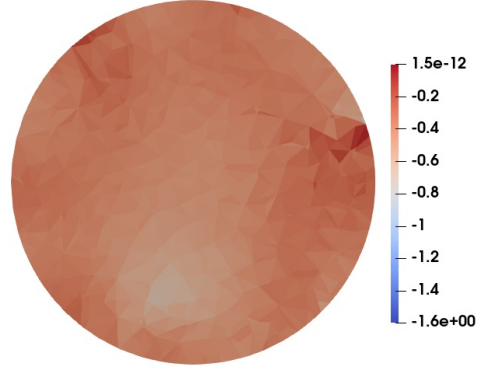
(a)



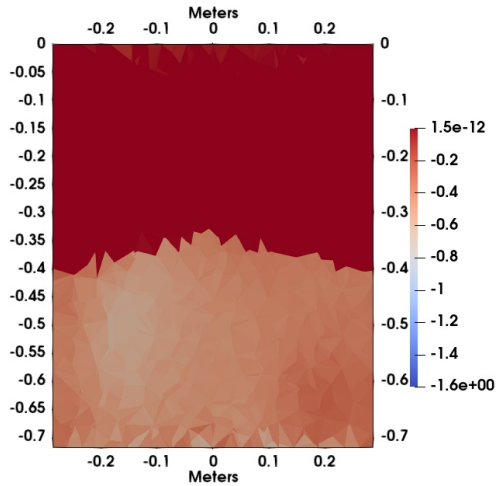
(b)



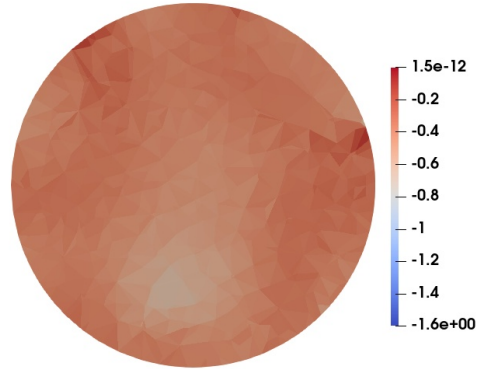
(c)



(d)

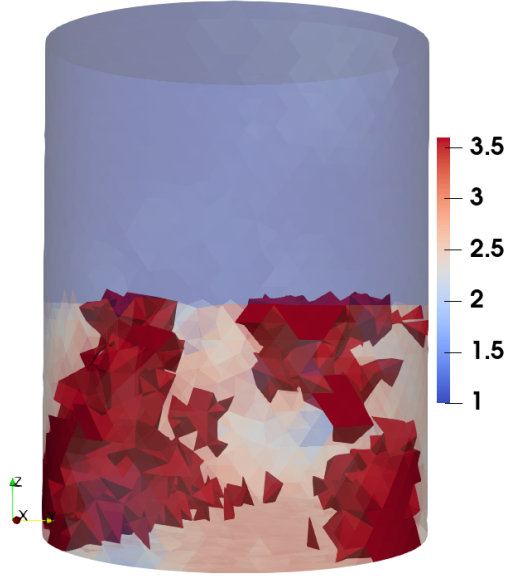


(e)

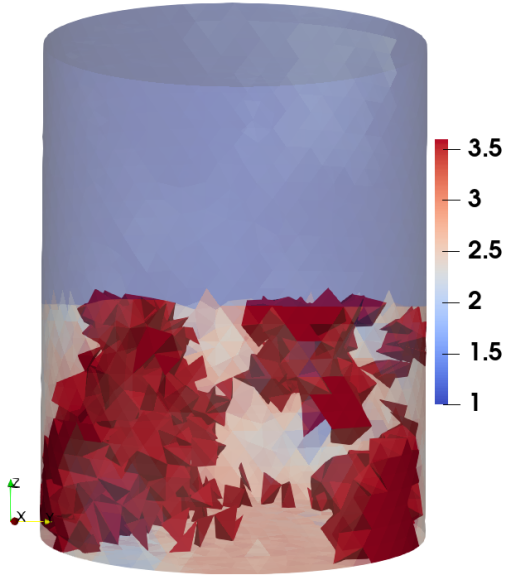


(f)

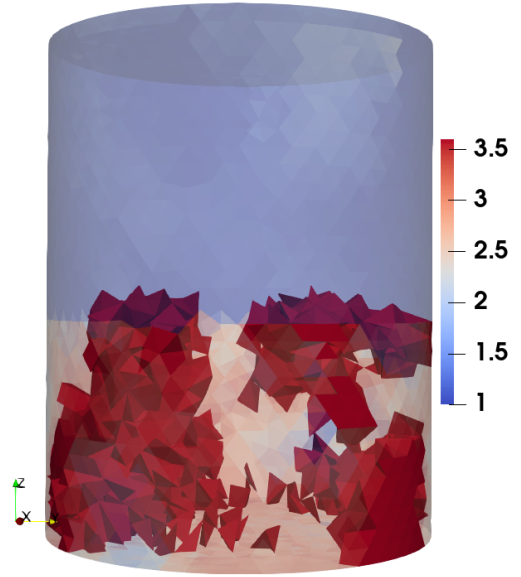
Figure 3.10: Traditional Calibrated Experimental FEM-CSI imaging results of $Im(\epsilon)$ for the frequency band 200MHz. Traditional calibration (a) vertical and (b) horizontal slice at 260MHz, (c) vertical and (d) horizontal slice at 270MHz, and (e) vertical and (f) horizontal slice at 280MHz.



(a)



(b)



(c)

Figure 3.11: One-Shot Calibrated Experimental FEM-CSI inversion 3D images of $Re(\epsilon)$ with a threshold at the frequencies of (a) 260MHz, (b) 270MHz, and (c) 280MHz. All tetrahedrons beyond a threshold of 3.6 are solid.

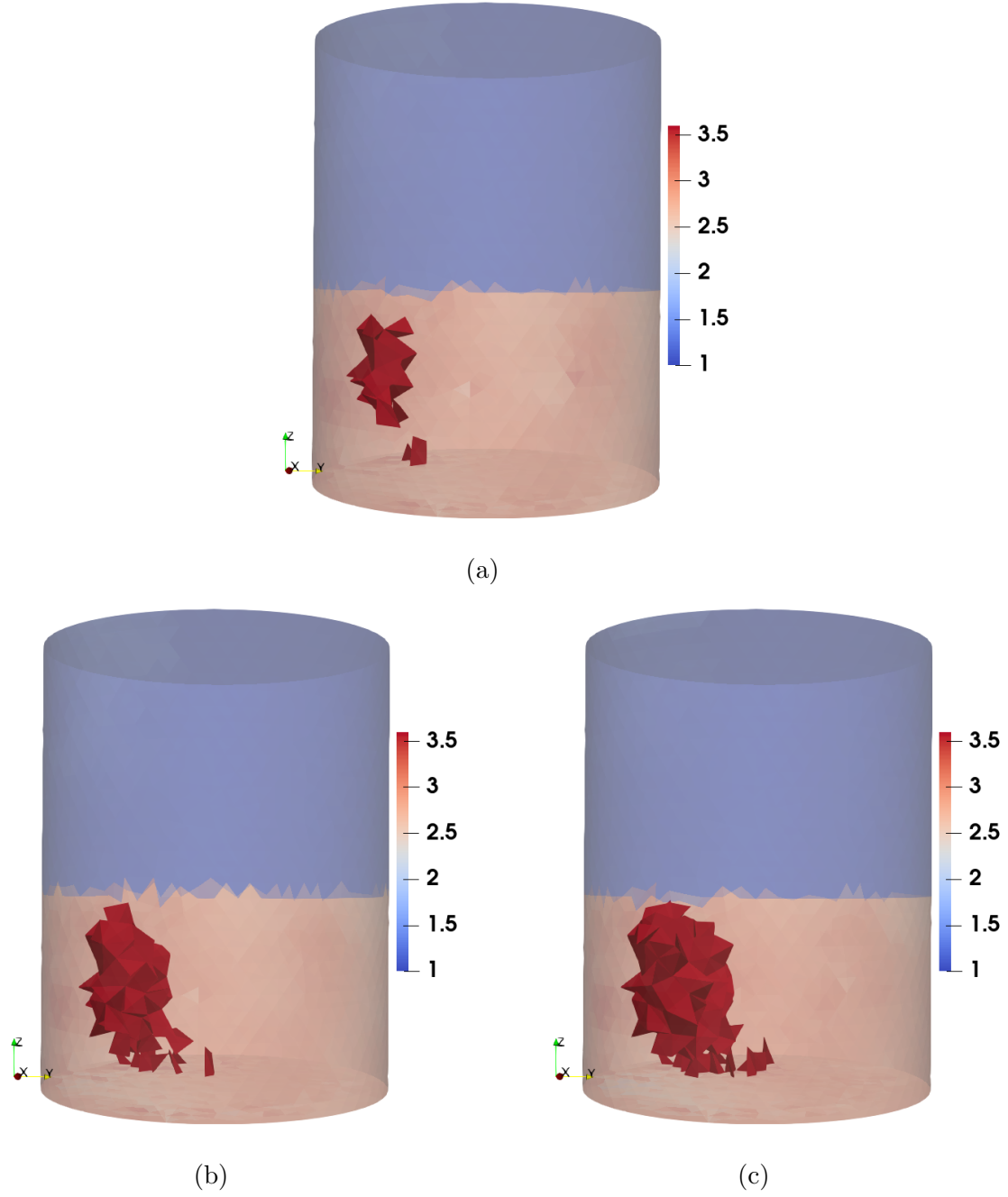
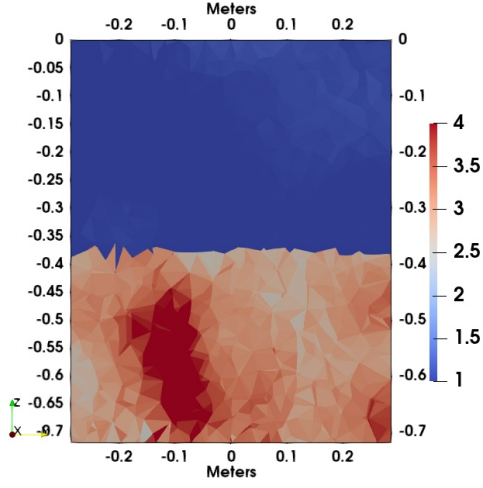
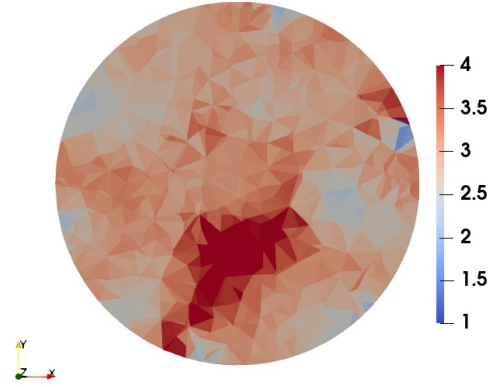


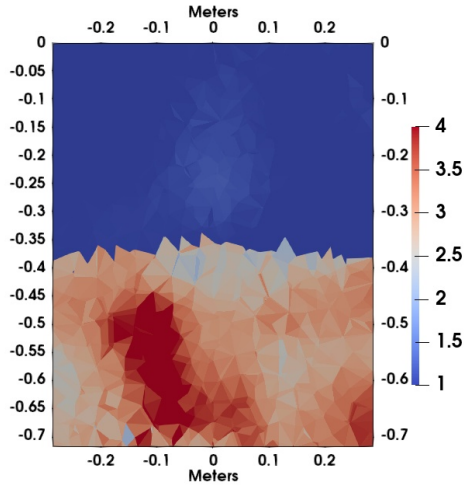
Figure 3.12: Traditional Calibrated Experimental FEM-CSI inversion 3D images of $Re(\epsilon)$ with a threshold at the frequencies of (a) 260MHz, (b) 270MHz, and (c) 280MHz. All tetrahedrons beyond a threshold of 3.6 are solid.



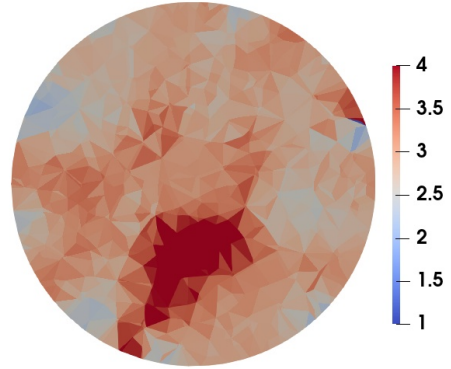
(a)



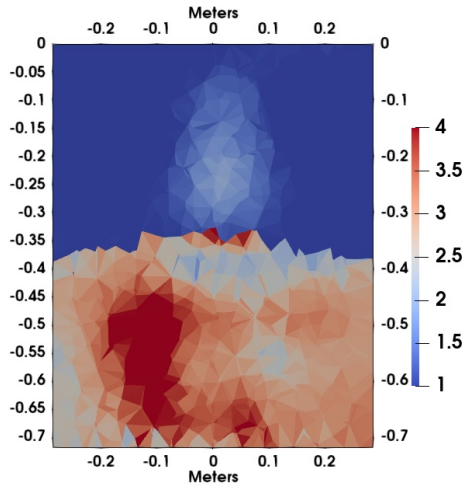
(b)



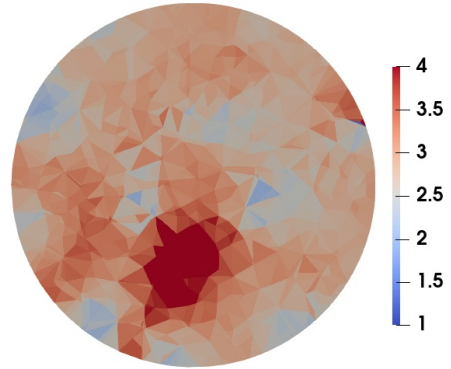
(c)



(d)

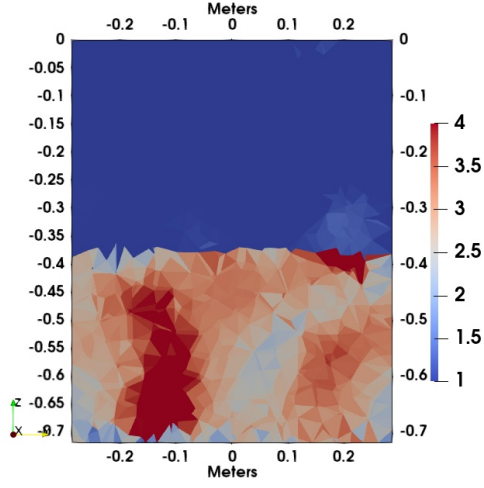


(e)

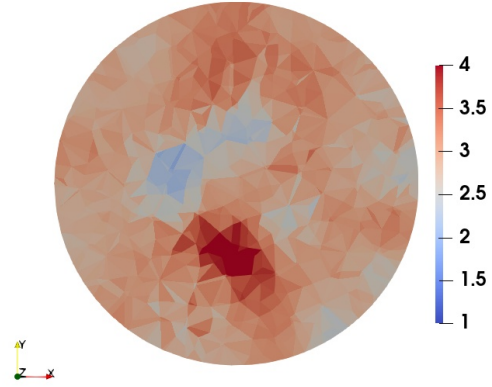


(f)

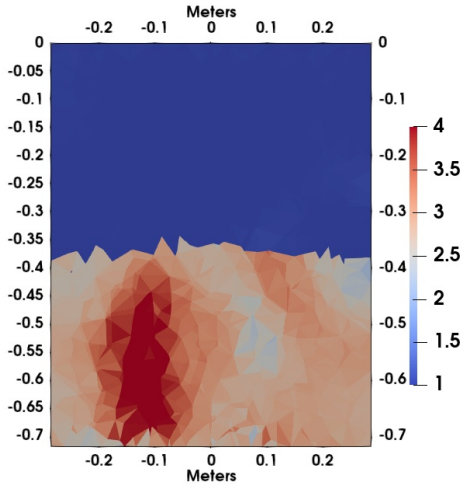
Figure 3.13: One-shot Calibrated Experimental FEM-CSI imaging results of $Re(\epsilon)$ for the frequency band 500MHz. Traditional calibration (a) vertical and (b) horizontal slice at 550MHz, (c) vertical and (d) horizontal slice at 560MHz, and (e) vertical and (f) horizontal slice at 570MHz.



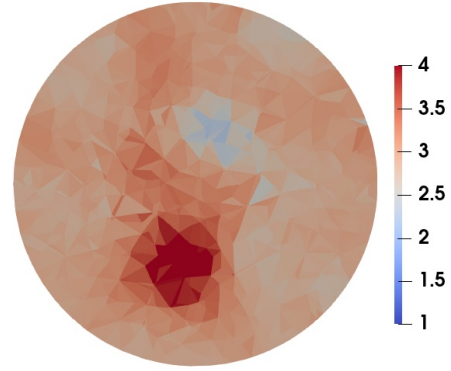
(a)



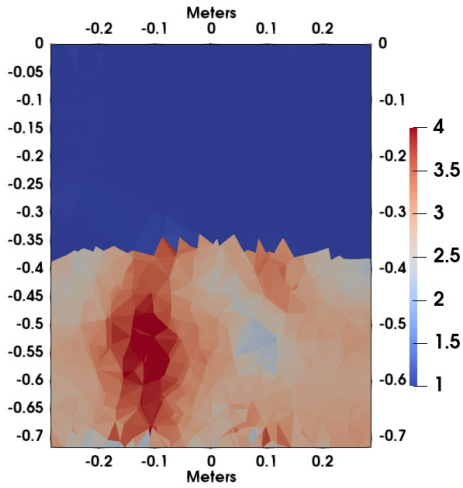
(b)



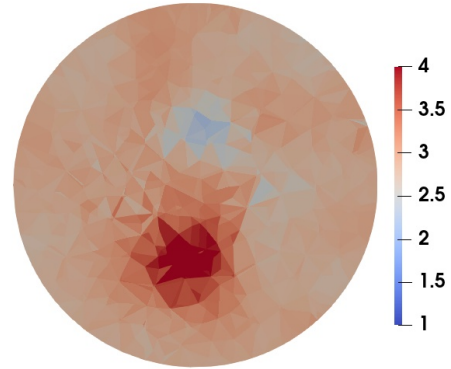
(c)



(d)

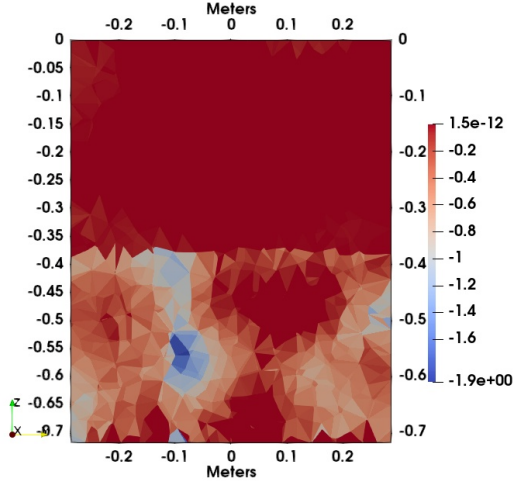


(e)

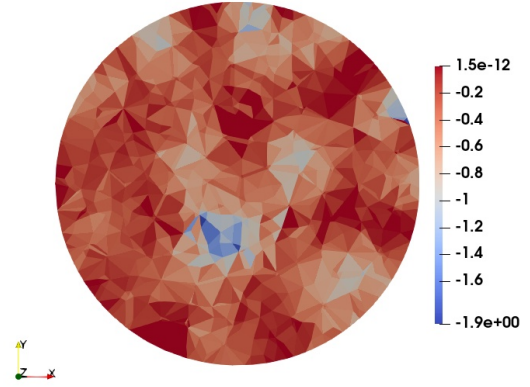


(f)

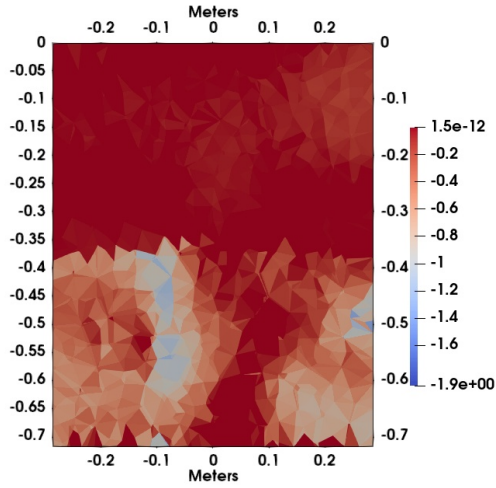
Figure 3.14: Traditional Calibrated Experimental FEM-CSI imaging results of $Re(\epsilon)$ for the frequency band 500MHz. Traditional calibration (a) vertical and (b) horizontal slice at 550MHz, (c) vertical and (d) horizontal slice at 560MHz, and (e) vertical and (f) horizontal slice at 570MHz.



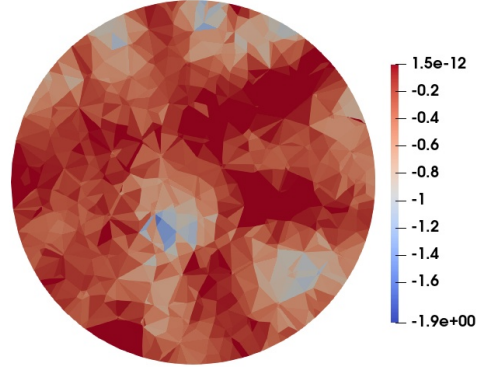
(a)



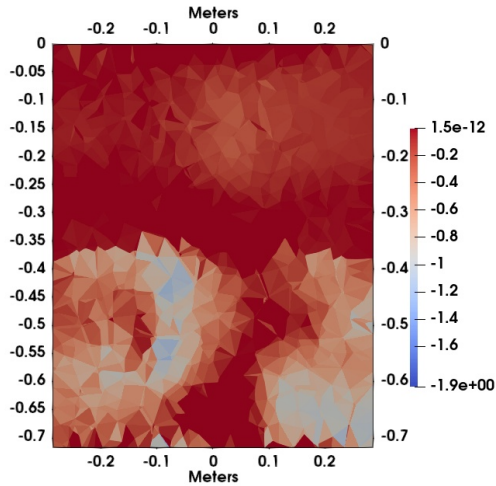
(b)



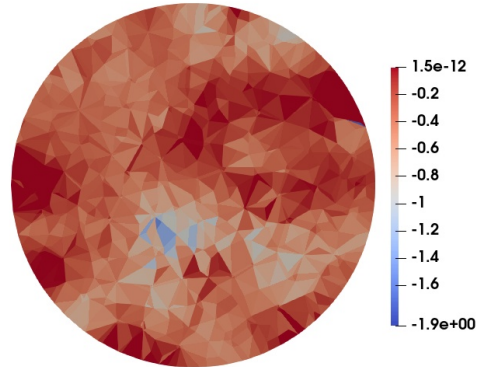
(c)



(d)

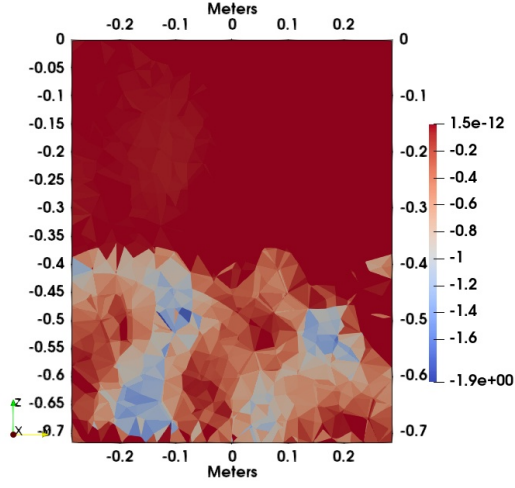


(e)

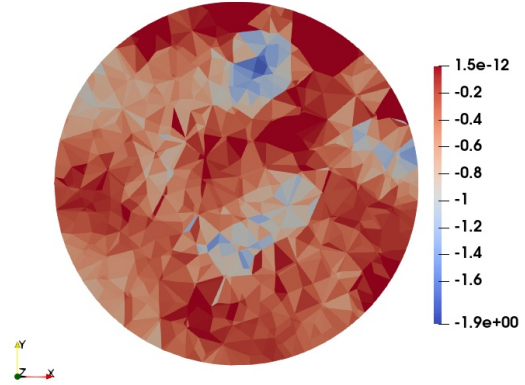


(f)

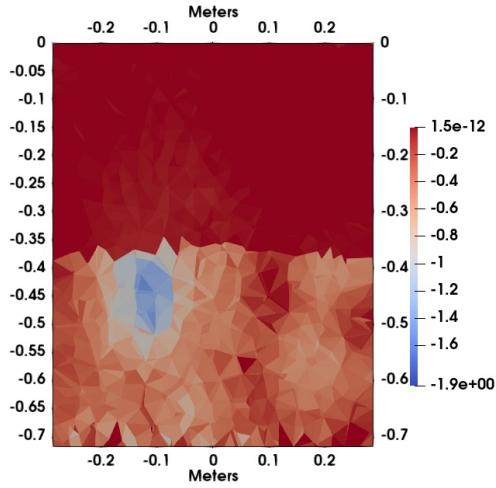
Figure 3.15: One-shot Calibrated Experimental FEM-CSI imaging results of $Im(\epsilon)$ for the frequency band 500MHz. Traditional calibration (a) vertical and (b) horizontal slice at 550MHz, (c) vertical and (d) horizontal slice at 560MHz, and (e) vertical and (f) horizontal slice at 570MHz.



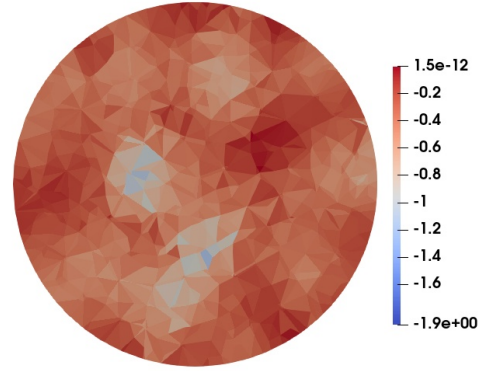
(a)



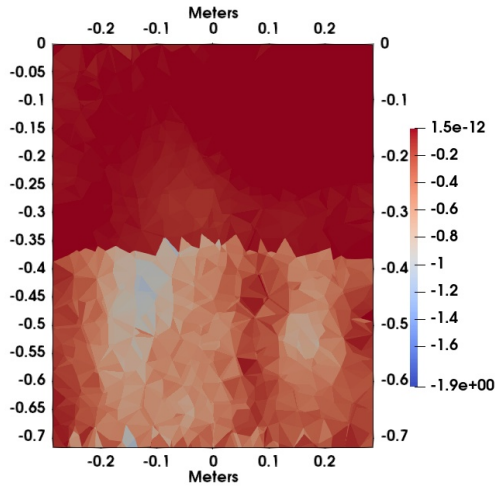
(b)



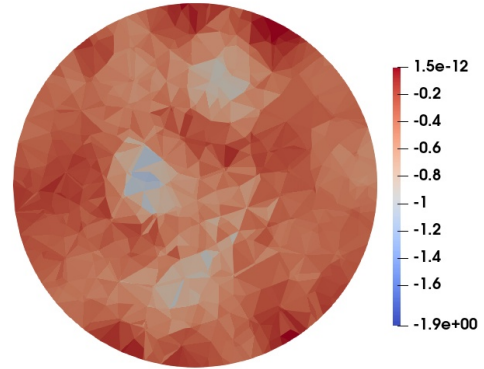
(c)



(d)

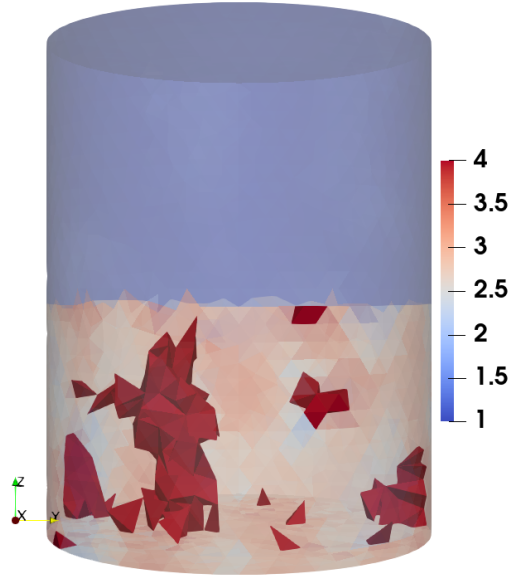


(e)

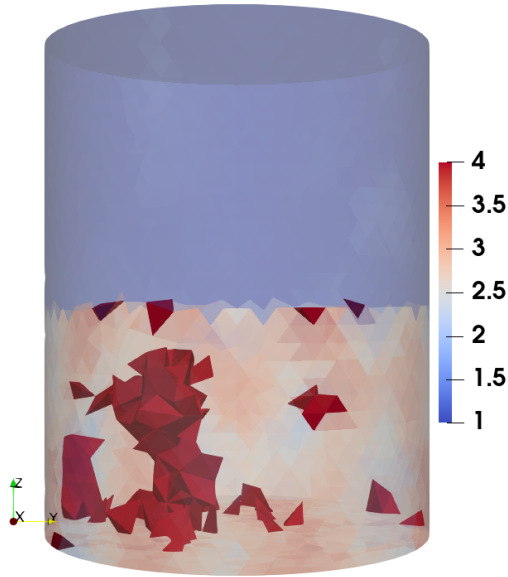


(f)

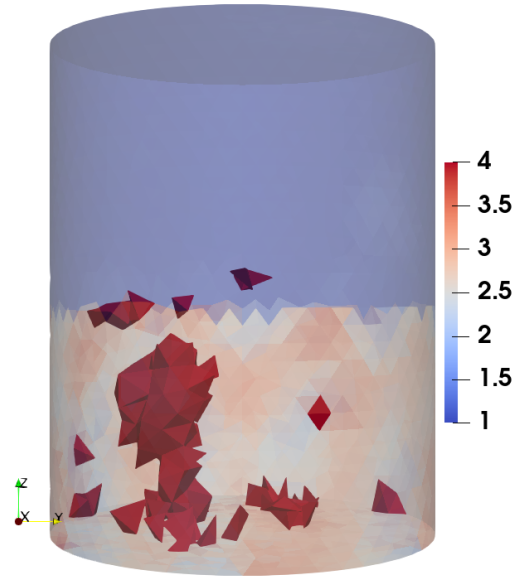
Figure 3.16: Traditional Calibrated Experimental FEM-CSI imaging results of $Im(\epsilon)$ for the frequency band 500MHz. Traditional calibration (a) vertical and (b) horizontal slice at 550MHz, (c) vertical and (d) horizontal slice at 560MHz, and (e) vertical and (f) horizontal slice at 570MHz.



(a)

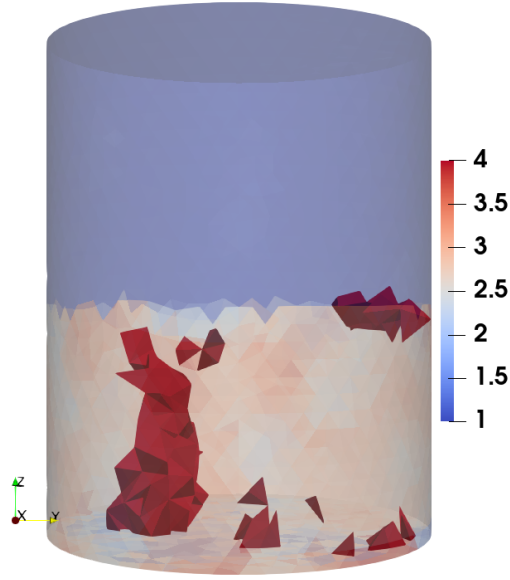


(b)

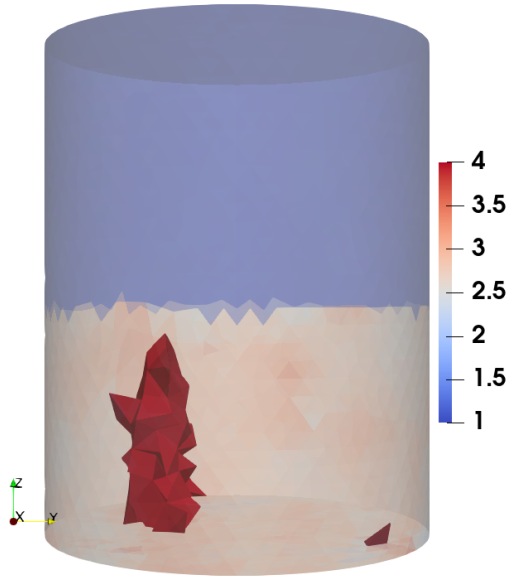


(c)

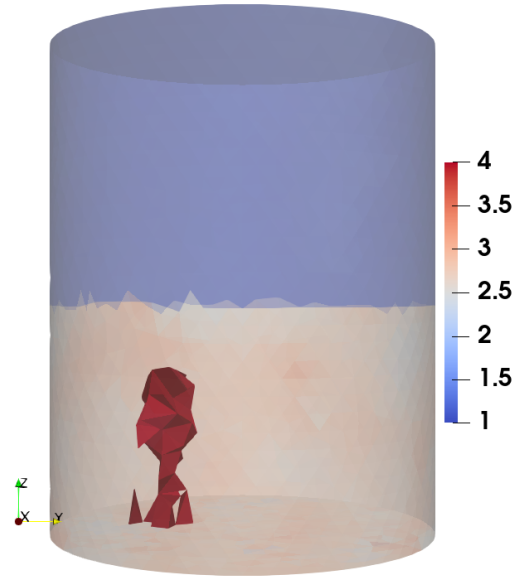
Figure 3.17: One-shot Calibrated Experimental FEM-CSI inversion 3D images of $Re(\epsilon)$ with a threshold at the frequencies of (a) 550MHz, (b) 560MHz, and (c) 570MHz. All tetrahedrons beyond a threshold of 4 are solid.



(a)



(b)



(c)

Figure 3.18: Traditional Calibrated Experimental FEM-CSI inversion 3D images of $Re(\epsilon)$ with a threshold at the frequencies of (a) 550MHz, (b) 560MHz, and (c) 570MHz. All tetrahedrons beyond a threshold of 4 are solid.

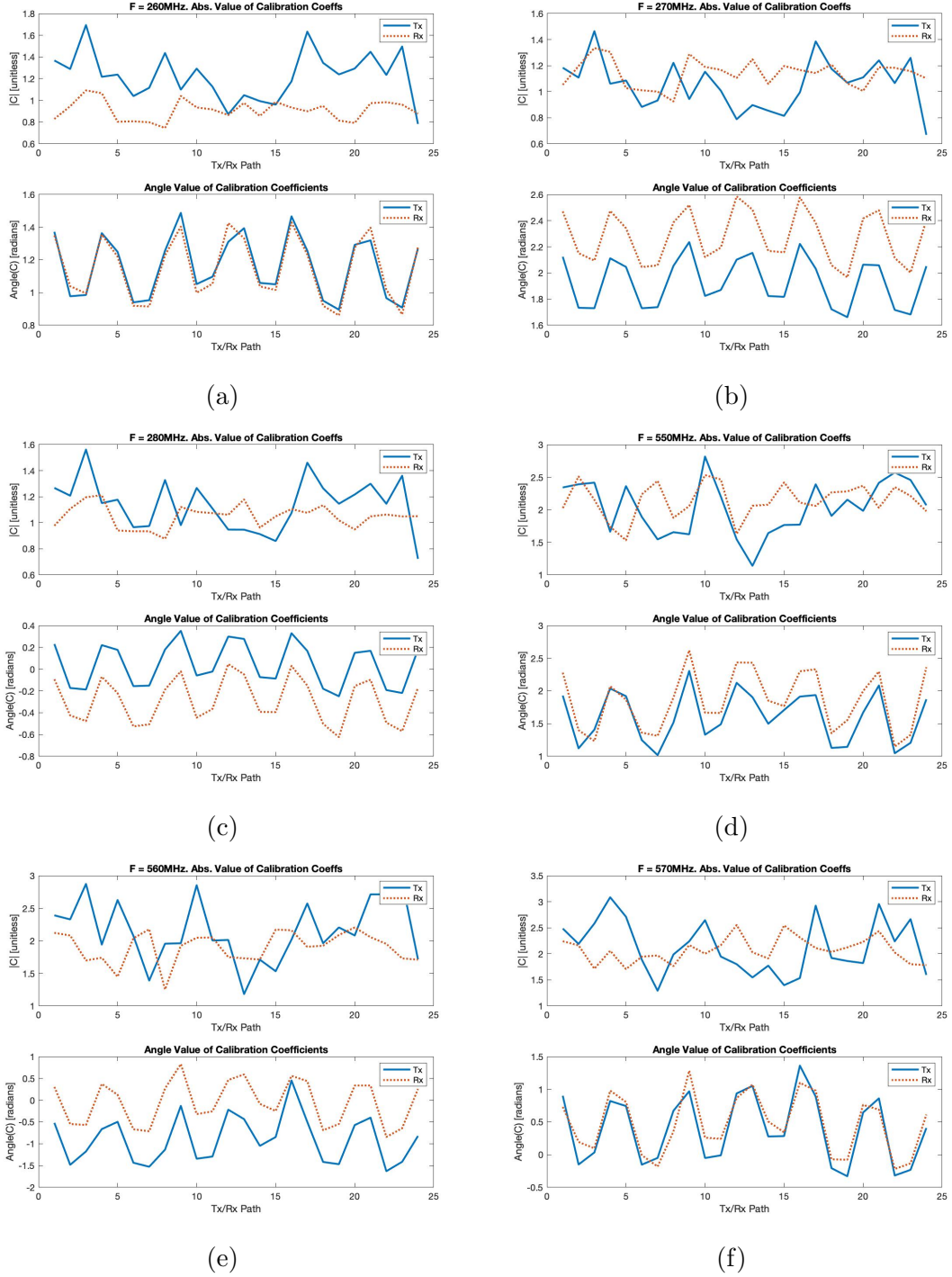


Figure 3.19: Calibration coefficient by transmit/receive path (or channel). (a) 260MHz (b) 270MHz (c) 280MHz (d) 550MHz (e) 560MHz (f) 570MHz. The coefficients in transmit mode are in blue (Tx), in receive mode are in red (Rx).

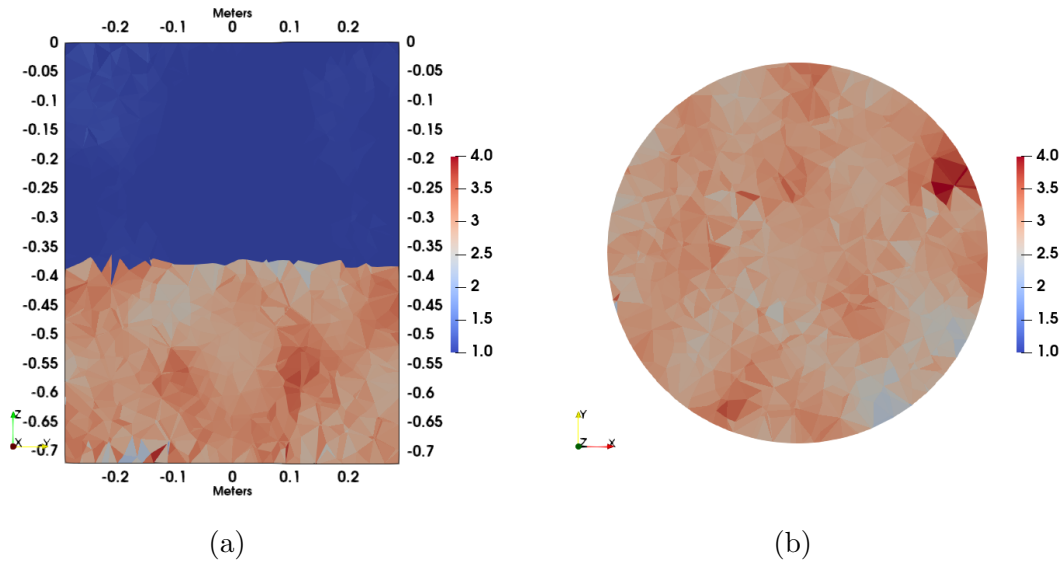


Figure 3.20: One-shot Calibrated Experimental FEM-CSI imaging results of $Re(\epsilon)$ using the measurements without a wet-grain target for 550MHz. Without target (a) vertical and (b) horizontal slice. This image can be compared with Fig 3.13(a) and (b), where the target was present.

3.5 Discussion for the Small Bin

A careful comparison of the traditional calibration and one-shot calibration images allows qualitative assessment of the proposed calibration technique. Overall, the single-shot images closely resemble the images obtained by applying the more traditional calibration procedure, but have more image artifacts, particularly in the lower frequency band. Degradation in the one-shot calibrated images is most clear in the 3D threshold images at the lower 250 MHz frequency band. We expect some degradation with one-shot as the traditional differential calibration procedure creates zero signal from anything that is common between the two measurements. Thus, there is no direct signal from any model imperfections (i.e, the physical barrel is different from the computational model), or the fact that the bulk grain may be (whereas our initial model is homogeneous), etc. Our proposed one-shot calibration technique leads to signals that contain scattered field from all of these differences. These extra scattered fields mean the final images will not be as high quality when detecting a wet-grain target. An example of the image degradation we can expect is shown for the no-target case in Fig. 3.20. We discuss this more extensively in Section 3.5.1 below.

In all images the ROC location is detectable, but the size of the ROC is larger at lower frequencies. This is expected as the target is quite small compared with the wavelength in the lower band (for example, wavelength of 260 MHz is 0.7 m, and the target dimensions are about 0.14 m maximum). It makes sense that the ROC is more distinguishable in the images with frequencies in the higher band due to the improved resolution available at higher frequencies. This is true for both one-shot and traditional calibration.

We also note that the cone angle in the traditional calibration images appears to be different from the one-shot image. The explanation of this difference is that the parameters \underline{p} are created with S^{known} for traditional calibration whereas $S^{unknown}$ is used for one-shot calibration. As the grain is homogeneous in S^{known} , and our parametric model assumes a homogeneous grain mass, this is a bias towards the traditional calibration providing more accurate images. While we could have used the parameters from $S^{unknown}$ for the traditional calibration as well, we chose not to as we wanted to test the one-shot algorithm against the best case traditional calibration. Our results show that even with this bias, the proposed algorithm still performs comparably to the traditional case.

3.5.1 Comparison of Computational Modelling Error in One Shot and traditional Calibration

To further emphasize our claims that the modelling error results in higher levels of noise (and thus worse final images) for the one-shot calibration method vs. traditional calibration, consider the case where we have modelling errors in the computational model. For example, errors in diameters, height of the bin, or the \underline{p} . Consider:

$$H(\underline{p}) = H^{ideal}(\underline{p}) + H^{error} \quad (3.5)$$

where $H(\underline{p})$ are the fields we obtain from the parametric inversion and $H^{ideal}(\underline{p})$ are the ideal fields for the perfect case (i.e. if we had a perfect computational model of everything in the bin), and H^{error} are the errors caused by our computational model/experimental system mismatch.

If we put these fields into our equation 3.3:

$$\begin{aligned} H_{xy}^{sct} &= C_x S^{unknown} C_y - H(\underline{p}) \\ &= C_x S^{unknown} C_y - H^{ideal}(\underline{p}) - H^{error} \\ &= H_{xy}^{sct,one} - H^{error} \end{aligned} \quad (3.6)$$

Where we have listed the ‘ideal’ scattered fields for the one-shot calibration method as $H_{xy}^{sct,one}$. Since the fields H_{xy} are the scattered fields sent to the inverse solver, the H^{error} fields are added directly to the scattered fields sent to the inverse solver and are not scaled in any way⁵.

⁵In addition to this problem, the modelling errors would lead to less accurate C_x and C_y coefficients, which would lead to even more error.

However, consider the traditional calibration Equation 2.17:

$$\begin{aligned}
H_{xy}^{sct,cal} &= \left(\frac{H(\underline{p})}{S_{xy}^{known}} \right) (S_{xy}^{unknown} - S_{xy}^{known}) \\
&= \left(\frac{H^{ideal}(\underline{p}) + H^{error}}{S_{xy}^{known}} \right) (S_{xy}^{unknown} - S_{xy}^{known}) \\
&= \left(\frac{H^{ideal}(\underline{p})}{S_{xy}^{known}} \right) (S_{xy}^{unknown} - S_{xy}^{known}) + \left(\frac{H^{error}}{S_{xy}^{known}} \right) (S_{xy}^{unknown} - S_{xy}^{known}) \\
&= H_{xy}^{sct,trad} + H^{error} \left(\frac{S_{xy}^{unknown} - S_{xy}^{known}}{S_{xy}^{known}} \right)
\end{aligned} \tag{3.7}$$

where we have listed the ‘ideal’ scattered fields for traditional calibration as $H_{xy}^{sct,trad}$.

The key difference is that the error term in the traditional case is *scaled by the subtraction of the S_{xy}^{known} and $S_{xy}^{unknown}$ measurements*. Since S_{xy}^{known} and $S_{xy}^{unknown}$ are close to each other, the modelling error is reduced with traditional calibration compared to one-shot calibration. For example, for the small bin example above at 550MHz (average over all transmit/receive pairs), the value of $|S_{xy}^{unknown} - S_{xy}^{known}|/|S_{xy}^{known}|$ is 0.33 with a median of 0.21.

All of this leads to the conclusion that one-shot calibration requires much lower levels of modelling error than traditional calibration in order to work. This conclusion is emphasized in the next section, where we consider an experiment in a much larger bin.

3.6 Experimental Results for a Large Grain Bin

The one-shot calibration technique proves to work for small scaled bins. We have tried data sets from various experimental bins. However, to date, the method is unable to obtain reliable images when tested on the detection of a small ROC in larger bins. In this section, some of the images obtained from a larger bin data set will be provided and discussed.

The data sets for this experiment were retrieved from a hopper style grain bin which had a volume of 90,000 liters (~ 2550 bushels) with dimensions of 7.35 m in height with a diameter of 4.7 m, and it is larger bin compared to previous bin (a height of 0.81 m and a radius of 0.56 m). Wheat grain was stored in the bin and it was filled to 2.48 m from the bottom of bin wall where the wall meets bottom cone of the bin. The top surface of the filled grain was flat. The details and schematic of this particular bin are shown in Fig 3.21. The installation method for antennas and connections to VNA follows the same configurations presented in Section 3.2 (e.g. [30, 39–43] and others) and we used the same data set that was used in [14].

An artificial target, a bag of wet grain that contains 29 % moisture content, was planted into the grain. This target was buried 0.81 m down from the grain surface near the bin wall. The diameter of the target is about 50 cm, the height is 44.5 cm, and the grain weighed about 63.5 kg, with a total volume of approximately 100 L. We chose 80, 90, and 100 MHz. Two sets of measurements are collected. The first set of measurements was taken before a wet grain target is planted and it is S^{known} . The second set was obtained after the target is planted and left in the grain for a day, this is $S^{unknown}$.

Before calibration, these data sets were preprocessed to ignore measurements that were obtained from some channels due to noise of unknown origin that limited data from certain antenna pairs. To determine the channels to be ignored, two sets of S measurements were taken back-to-back with the ROC placed into the bin and the results were subtracted. The subtraction of the two signals should be low in every channel to be acceptable as good measurements since nothing changed in the bin during the two scans, any changes in signal must be noise. The difference of two signals are converted to decibels $20 * \log_{10} |S_{21_1} - S_{21_2}|$. Then, we ignored channels where the dB of the difference is higher than -70 dB (most differential signals were below -100 dB). When a antenna has more than 40 % of its channels ignored, the whole antenna is ignored (antenna 13 and 14

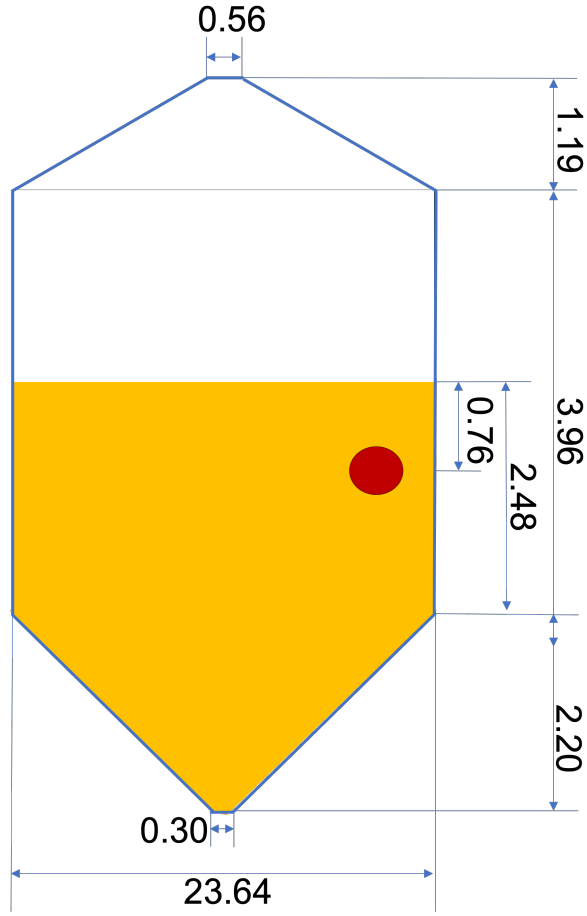


Figure 3.21: Layout of hopper style grain bin for synthetic test. The permittivity of the grain is $4.5 + j0.35$ at 90MHz (18% moisture content) while the permittivity of the ROC is $7 + j0.75$ at 90MHz (29% moisture content) [38].

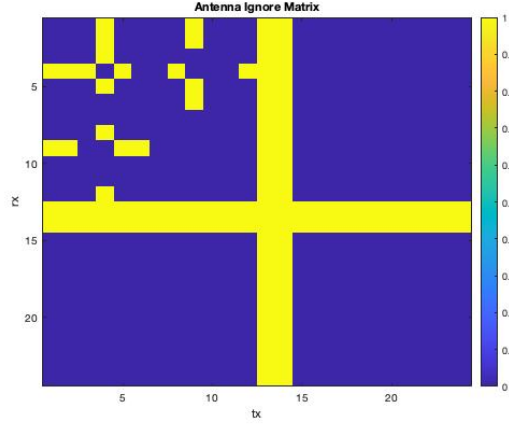


Figure 3.22: The yellow shows the antennas that are ignored. The whole antenna 13 and 14 are discarded.

Table 3.2: Results of parametric inversion for each frequency, large bin

Frequency (MHz)	ε_{rel}	Est. Height (from the eave top, meters)	Est. Angle (degree)
80	4.53 - $j0.49$	0.62	-0.12
90	4.59 - $j0.54$	0.57	0.02
100	4.56 - $j0.48$	0.61	0.08

in our experiment). The channels that were ignored are shown in Fig. 3.22.

Following the workflow proposed and explained in the previous chapter, we produced the 3D images of real permittivity of the grains. Other than ignoring certain antenna pairs, as described above, the workflow for the large bin was identical to the barrel test outlined previously. Same as the images that were presented in the previous chapter, these images are 2D vertical slices of real permittivity and are compared with the images generated with traditional calibration. These images are shown in Fig. 3.23. Additionally, the 4 parameters that were estimated from parametric inversion are reported as reference in Table 3.2.

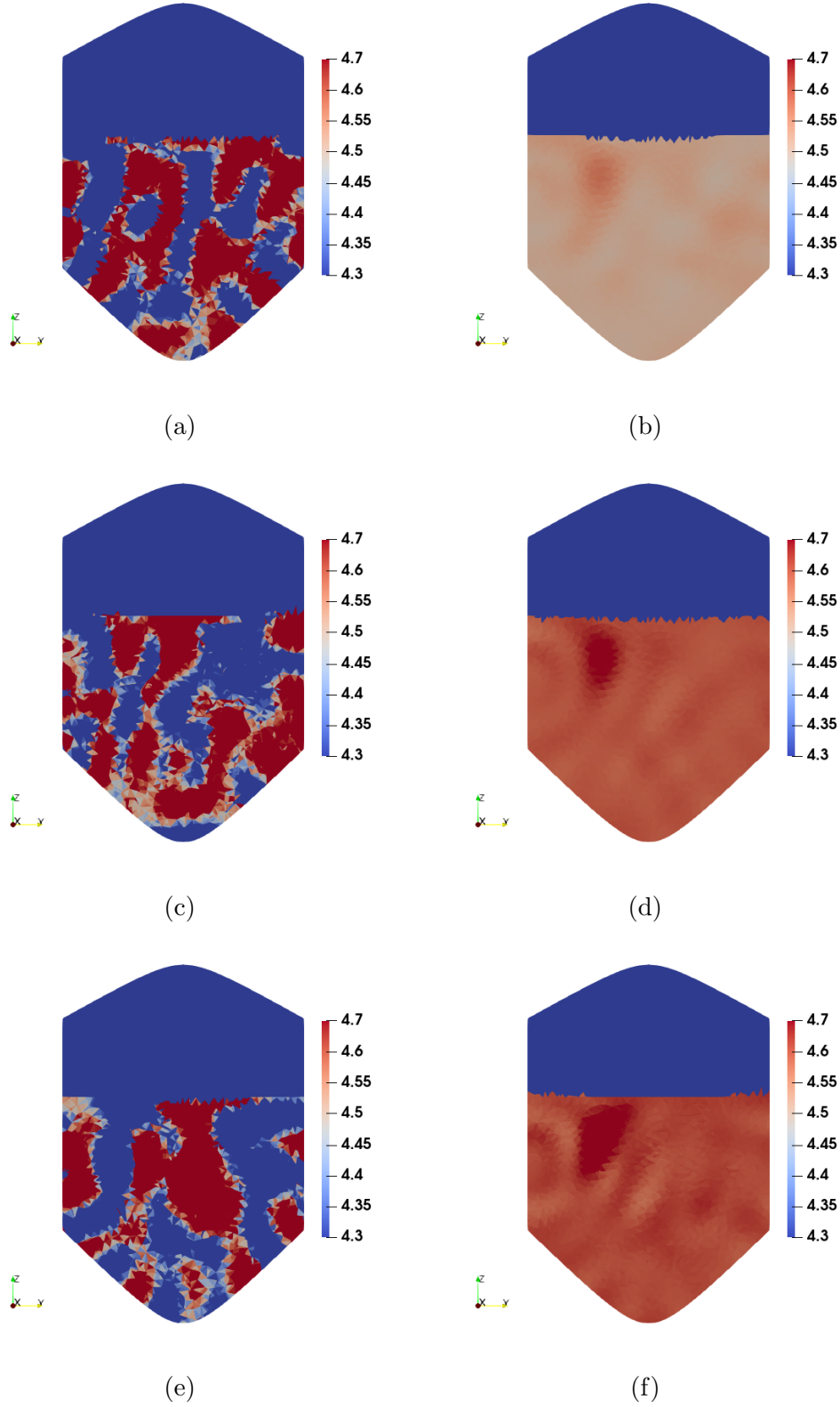


Figure 3.23: 2D vertical slices of the FEM-CSI result for single-shot vs traditional calibration on datasets collected from industrial scale bin. Sliced images for one-shot calibration (a), (c), and (e) are 80MHz, 90MHz, and 100MHz accordingly. Sliced images for traditional calibration (b), (d), and (f) are 80MHz, 90MHz, and 100MHz accordingly

3.7 Discussion for the Large Bin

Unlike the results from the small bin experiment, we could not locate the a ROC in using the proposed one-shot calibration procedure, while the ROCs were recoverable in traditionally calibrated images. The exact reason for these results is still unclear, but herein we discuss a few possibilities that could cause this difference between small and large bins.

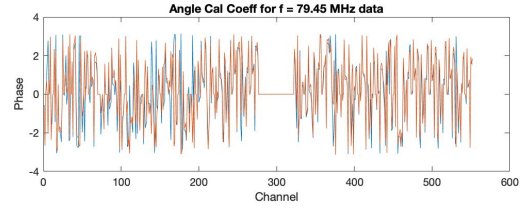
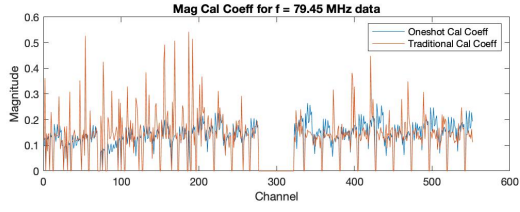
The most likely explanation is that the modelling errors are too large as it is discussed in Section 3.5.1. Traditional calibration's Modelling errors are reduced greatly. Average value of $|S_{xy}^{unknown} - S_{xy}^{known}|/|S_{xy}^{known}|$ is 0.09 with a median of 0.04 at 90MHz. The inversion algorithm cannot account for the modelling error in any way but an erroneous image, causing the resulting image to fail.

The data collected and used for this experiment is not the most recent hardware revision, nor was the installation process the one that is currently used in practice. The reason for using the old system was because this is the only the data set that the ROC is detectable for large bin experiment. However, this system uses outdated configurations of cables and antennas that might introduce noise. This can add more errors in the model and this is shown in images as in Fig. 3.23.

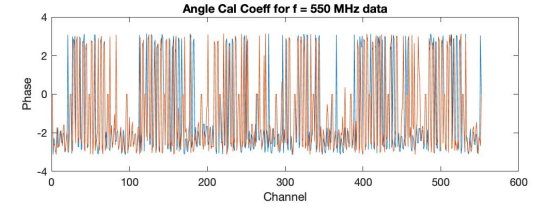
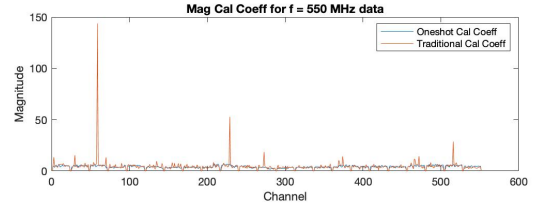
For further analysis, we supplemented 3 sets of plots that could show the performance of one-shot calibration. These plots are created to show calibration coefficients, total field (H^{tot}), and scattered field (H^{scat}) at each channel (transmit 24 and receive 23, total channel 552) presenting both the one-shot and traditional calibration together. The plots are created for selected frequencies (80, 90, and 100 MHz), and compared to 550, 560, and 570 MHz from a small bin data set. The total field, H^{tot} , is obtained for traditional calibration by the multiplication of the calibration coefficients and $S^{unknown}$. However, the counterpart of H^{tot} for one-shot calibration is defined as $C_x \cdot S \cdot C_y$.

In these plots, if the one-shot calibration will work to find the ROC, the plot of one-shot calibration is expected to follow closely to the plot of traditional calibration. The plot of calibration coefficient is shown in Fig. 3.24. We could not find noticeable evidence of a performance issue in the calibration coefficient plots. The only exception is a noticeable difference around channel 500 in (c). Total field and scattered field plots are shown in Fig. 3.25 and Fig. 3.26. After observation, one-shot's total field seems to follow traditional calibration in both the small and large bin scenarios, but interestingly,

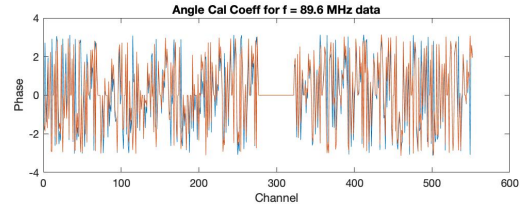
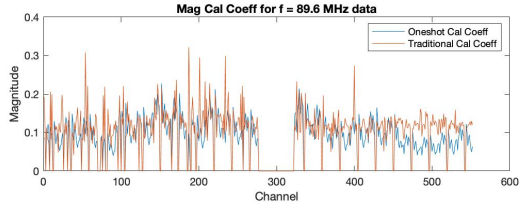
a large difference was observed in the scattered field. This is clearly shown in Fig. 3.26 comparing the left and right columns. In the large bin, the scattered fields are much larger for the one-shot case. This difference is caused by the errors in the model. These errors are observed to be greater for the large bin experiment when compared with the small bin case. This difference in the scattered field manifests itself as the erroneous images in the one-shot images shown in Fig. 3.23 (a),(c), and (e). Our conclusion from these plots is that, In order to obtain acceptable images, it is important to create a model that has as few errors as possible.



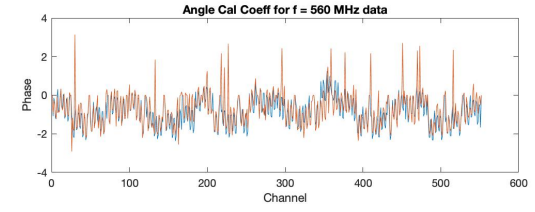
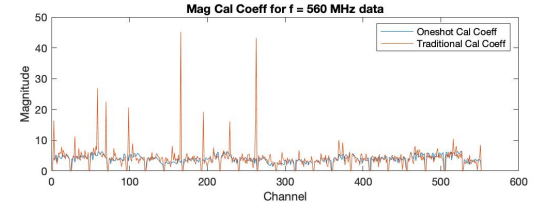
(a)



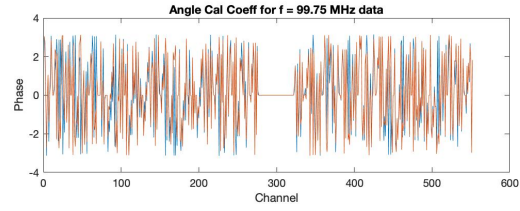
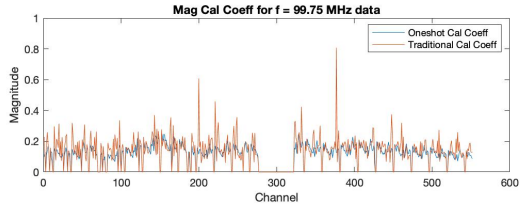
(b)



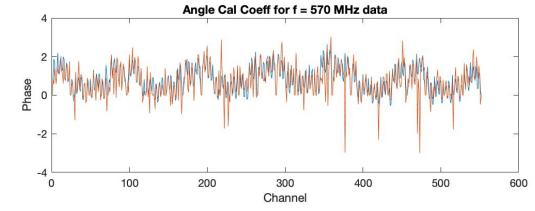
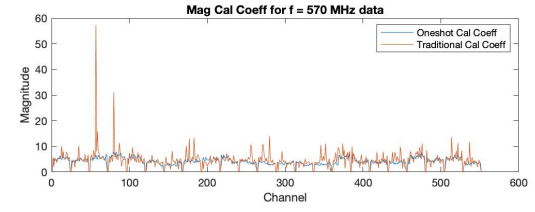
(c)



(d)

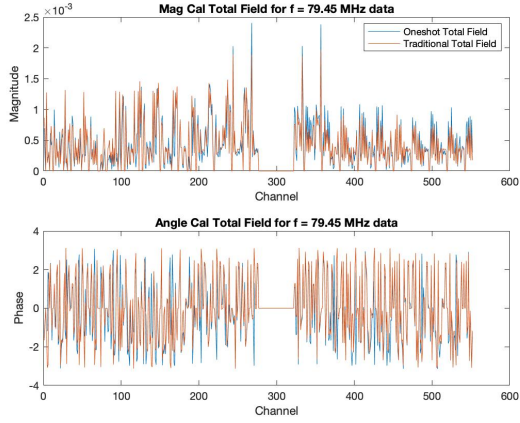


(e)

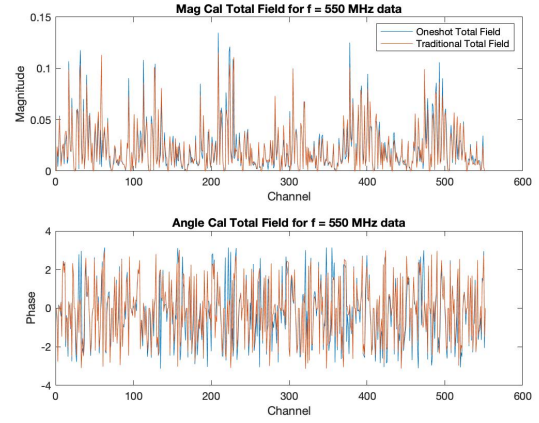


(f)

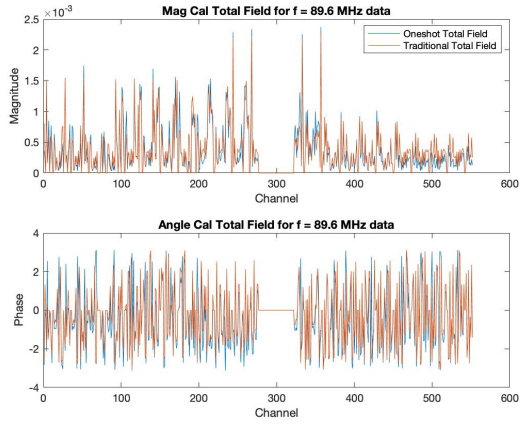
Figure 3.24: Calibration coefficients one-shot vs traditional method for (a) 80MHz, (c) 90MHz, (e) 100MHz of large bin comparing to (b) 550MHz, (d) 560MHZ, (f) 570MHz of small bin.



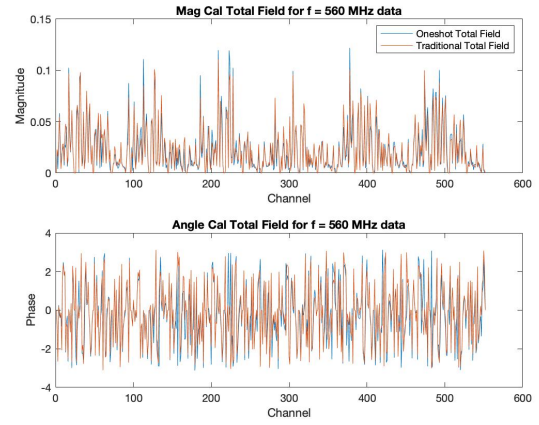
(a)



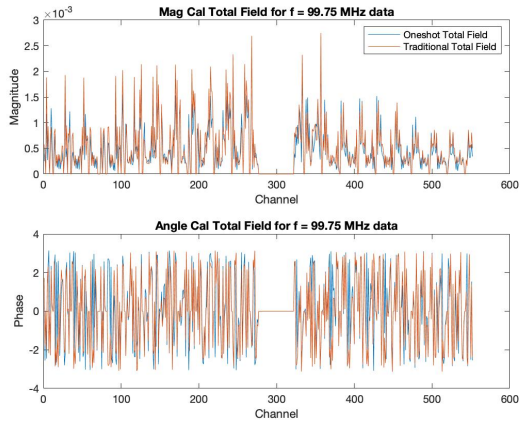
(b)



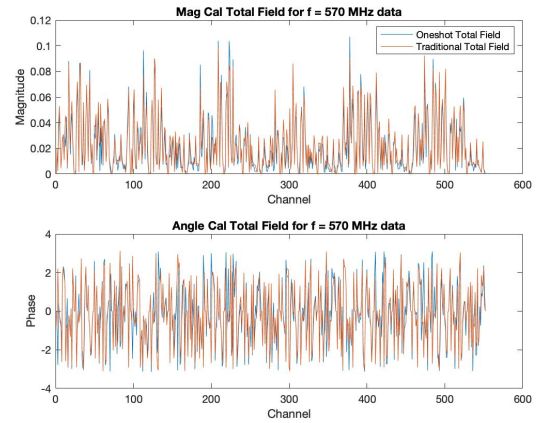
(c)



(d)

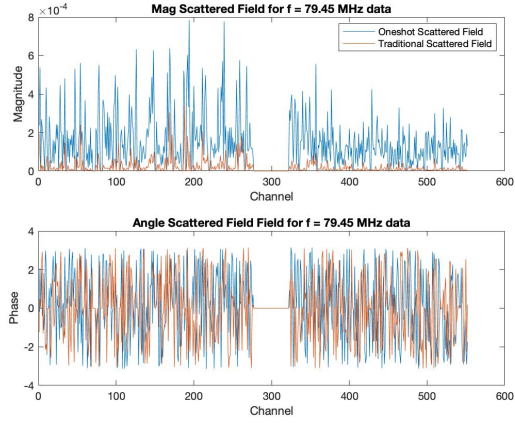


(e)

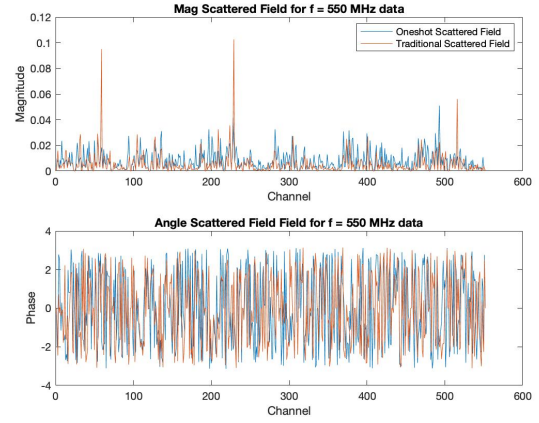


(f)

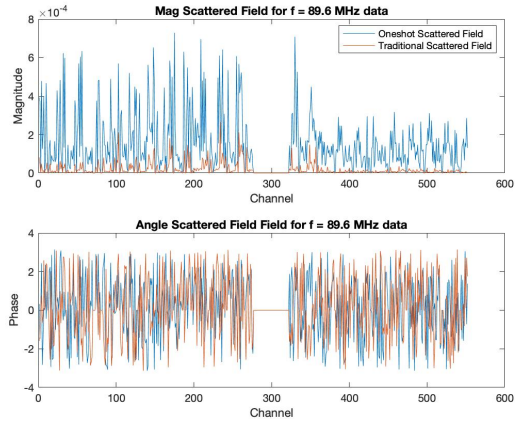
Figure 3.25: Total field obtained from small and large bin data sets. Left side is 80MHz, (b) 90MHz, and (c) 100MHz of large bin. Right side is (b) 550MHz, (d) 560MHz, and (f) 570MHz of small bin.



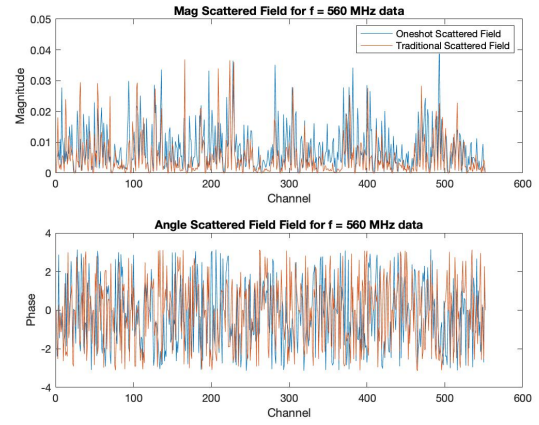
(a)



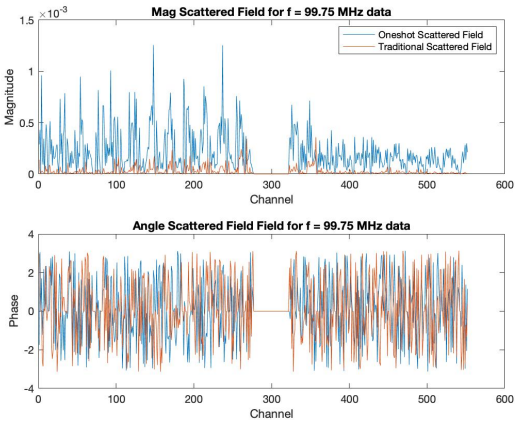
(b)



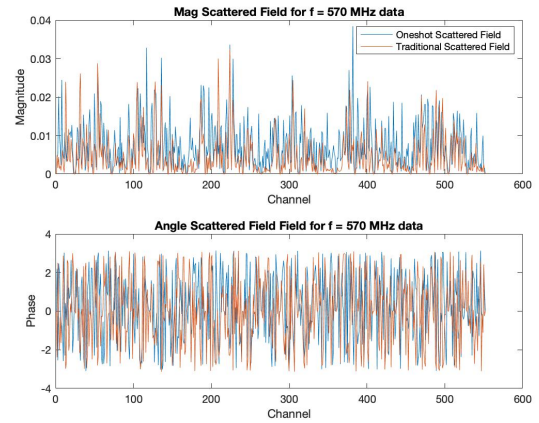
(c)



(d)



(e)



(f)

Figure 3.26: Scattered field from small and large bin data set. Left side is 80MHz, (b) 90MHz, and (c) 100MHz of large bin. Right side is (b) 550MHz, (d) 560MHz, and (f) 570MHz of small bin.

Chapter 4

Conclusion

In this work we have proposed, implemented, and tested a one-shot calibration procedure for electromagnetic imaging applied to uncooperative stored-grain imaging problems. The calibration procedure uses a parametric inversion technique to recover the bulk properties of the grain, from which a numerical model is constructed to represent a known target.

The key realization of our proposed method is that this parametric model can provide a set of H -fields that we can use as a target for an optimization algorithm. We then use a simple magnitude and phase-shift to model each transmit and receive path (a set of 48 complex-valued calibration coefficients) as our model of how the physical measurement system corrupts the desired signal measured directly at the antenna port. Given the simple model of calibration coefficients and the optimization target of the parametric fields, we are able to estimate these 48 coefficients via optimization.

The net effect in grain bins is that we can image inhomogeneous grain regions located in a mass of more homogeneous grain with a single measurement in an uncooperative EMI system. Previously, this process required at least two measurements and letting time elapse between the two measurements. In terms of practical benefit, grain handlers can now image inhomogeneous grain masses immediately after filling the bin.

We have demonstrated that the proposed single-shot calibration method works well for a synthetic example, where the images based on the one-shot procedure and the two data-set process are very similar. For a lab-scale experimental setup in a controlled environment, the results show that the procedure provides final images that are close, but slightly degraded compared to images from a two data-set calibration process. This degradation is acceptable as there is currently no other method for calibrating data in

uncooperative imaging systems such as grain bins.

On a larger experimental bin, the technique did not produce acceptable results. The most likely reason for this lack of results is that within the larger bin, the computer model does not fit the collected data as well. More speculations on this are given below in the future work section.

In conclusion, we claim that the one-shot calibration procedure shows great promise for industrial deployment. The basic components of the algorithm have been shown to be effective for experimental systems, and the use of a parametric inversion to provide a background, combined with a simple model of each transmit receive channel does model the system well enough. We have shown that under certain conditions, the procedure can eliminate the need for the second data set while showing a grain region of high moisture. This is a first to be able to calibrate and image on an experimental data set. However the results in the larger grain bin show that this process will require more research before it can be deployed in an industrial setting (discussed below).

4.0.1 Future Research

Given the results of this thesis, there are several areas that should be given consideration for future work. As stated in Chapter 3, it seems clear that the larger modelling errors in the larger bin are leading to a break-down of the one-shot calibration process in this large bin (and this can be expected to apply to other large bins as well). The exact reasons for the worse modelling error in the larger bin remain unclear. Future work on one-shot calibration should focus on ways to reduce this modelling error. One suggestion is to use better computational models of the antennas (e.g. modelling an actual antenna inside of the computational solver). Another area to consider would be to find a better initial model of the grain for the parametric solver. For example, in the large grain bin, it may be that the larger errors between the computational model and the physical system come because the grain in the bin is not actually homogeneous. The simple computational model of homogeneous grain with a given height and cone angle could be accurate inside of the small bin, but inaccurate for the large bin, where the larger amount of grain leads to inhomogeneities that are not modelled in the parametric solver. Examples of possible research might include the use of asymmetric grain surfaces in the initial model or the use of other basis functions that could capture more information about the initial state

of the grain (e.g. one could divide the grain into 5 different layers and seek an average permittivity for each). Whatever the process, the analysis herein indicates that this modelling error must be reduced before one-shot calibration could be widely deployed.

Another area of future research that should be considered is extending the single complex coefficient for each transmit and receive path in the transceiver system. Perhaps the best model of the transceiver would be a full 24-port calibration matrix, but this would be very difficult to obtain. However, it might be possible to use this one-shot approach with a 2-port model for each transmit-receive path (for a total of $48 \times 4 = 192$ complex coefficients). This 2-port model per channel would be a better match for the physics of how signals between the VNA and antenna port are corrupted by the presence of the measurement system. While it is not clear how much of an improvement one could expect, it is clear that a 2-port model would be more accurate.

Chapter 5

Source Code

Matlab source code for single-shot calibration is provided in this section. The code creates calibrated scattered field that is given to FEM-CSI algorithm.

```
clear all
close all
clc

%Read frequency file
freqFileLoc = ''
freqFile = 'frequencies.txt'
freqRead = dlmread([freqFileLoc freqFile], '\t');
fSim = freqRead/1e6; %units MHz.

numTx = 24;
numRx = 24;
numFx = length(fSim);

%Sometimes we may want to ignore certain antennas in the optimization. This
%can be very important if there are antennas that are not working well.
load('')

%Location of the H-para1 and H-para2 fields (i.e. parametric inversion
%results)
nelderMeadFieldsLoc1 = ''
```

```

nelderMeadFieldsLoc2 = ''

%location of measurement (i.e. S^unknown and S^known)
dataSetToImageLocation = ''
%file name of S^unknown
dataToImageFileName = ''
%file name of S^known
dataToIncFilename = ''

%In order to convert Hx,Hy,Hz fields from Hphi (And vice-versa)
%we need to the rxFile (and the field projections associated with each)
rxFile = 'RxFile.txt'

%This is just to point to our output directory where we will save the
%total, scattered, and incident fields (both the exact/true and the
%calibrated fields).
outputDir = ''

ndmcount=1;
for fx = 1:length(fSim)

    %Read in the first parametric (nelder-mead) files.
    nelderMeadFieldsHxHyHz1 = dlmread([nelderMeadFieldsLoc1 'HtotObs'...
        num2str(ndmcount) '.dat']);
    ndmcount=ndmcount+1;

    %Convert the nelder-mead (parametric) input files from HxHyHz format to
    %Hphi format.
    if isempty(nelderMeadFieldsHxHyHz1)
        nelderMeadFieldsHxHyHz1 = zeros(552*3,1);
    else
        nelderMeadFieldsHxHyHz1 = nelderMeadFieldsHxHyHz1(:,1) + ...
            1i*nelderMeadFieldsHxHyHz1(:,2);
    end

    H_para1 = convertHxHyHzToHPhi(rxFile,nelderMeadFieldsHxHyHz1,numTx,numRx);

```

```

%Read in the second parametric (nelder-mead) files.
nelderMeadFieldsHxHyHz2 = dlmread([nelderMeadFieldsLoc2 'HtotObs' ...
    num2str(ndmcount) '.dat']);
ndmcount=ndmcount+1;

%Convert the nelder-mead (parametric) input files from HxHyHz format to
%Hphi format.
if isempty(nelderMeadFieldsHxHyHz2)
    nelderMeadFieldsHxHyHz2 = zeros(552*3,1);
else
    nelderMeadFieldsHxHyHz2 = nelderMeadFieldsHxHyHz2(:,1) + ...
        1i*nelderMeadFieldsHxHyHz2(:,2);

end
H_para_inc = convertHxHyHzToHPhi(rxFile,nelderMeadFieldsHxHyHz2,...
    numTx,numRx);

%Read in S^unknown and save to S1_data
[S_Mat_FullFreqs,freqs,sonar,dataDateTime] = ...
    readJSONTransceiverToMatlab([dataSetToImageLocation...
    dataToImageFileName],1);
[dummy, fIndex] = min(abs(freqs - fSim(fx)*1e6));
fIndex = fIndex;
actualFreq(fx) = freqs(fIndex);
ccount = 1;
S1_Data = zeros(numTx*(numRx-1),1);
for tx = 1:numTx
    for rx = 1:numRx
        if tx~=rx
            S1_Data(ccount) = S_Mat_FullFreqs(fIndex,tx,rx);
            ccount = ccount+1;
        end
    end
end

%Read in S^known and save to Sinc_data
[S_Mat_FullFreqs_1,freqs_1,sonar_1,dataDateTime_1] = ...
    readJSONTransceiverToMatlab([dataSetToImageLocation...
    dataToIncFilename],1);

```



```

[dummy_1, fIndex_1] = min(abs(freqs_1 - fSim(fx)*1e6));
fIndex_1 = fIndex_1;
ccount_1 = 1;
Sinc_Data = zeros(numTx*(numRx-1),1);
for tx = 1:numTx
    for rx = 1:numRx
        if tx~=rx
            Sinc_Data(ccount_1) = S_Mat_FullFreqs_1(fIndex_1,tx,rx);
            ccount_1 = ccount_1+1;
        end
    end
end

%Plot raw target data: S^unknown vs H_p
figure
subplot(2,1,1)
plot(abs(S1_Data));
hold on
plot(abs(H_para1), 'r--');
title('Raw Target Data (S1) and H_para');
ylabel('Magnitude');
legend('Target Data', 'H_{para}');
subplot(2,1,2)
plot(angle(S1_Data));
hold on
plot(angle(H_para1), 'r--');
ylabel('Phase')
title('Raw Target Data (S1) and H_{para}');

%Convert all these fields from vector format into a matrix
%format. This makes the C1*S1*C1 operation feasible in Matlab's
%optimizaiton package.
S1_DataMat = zeros(numTx,numRx);
H_para1Mat = zeros(numTx,numRx);
H_para_incMat = zeros(numTx,numRx);
Sinc_DataMat = zeros(numTx,numRx);

%Convert the vector to a matrix
count = 1;

```

```

for tx = 1:numTx
    for rx = 1:numRx
        if tx~=rx
            Sinc_DataMat(tx,rx) = Sinc_Data(count);
            H_para1Mat(tx,rx) = H_para1(count);
            H_para_incMat(tx,rx) = H_para_inc(count);
            S1_DataMat(tx,rx) = S1_Data(count);
            count = count+1;
        end
    end
end

%Normalize the optimization cost functional with these
tempNorm1 = norm(H_para1Mat);

%The initial guess.
Cinitial = rand(4*numTx,1);

%Our cost functional for the || C S_corrupted C - H_parametric ||^2
func1 = @(C) (norm((1-ignoreMat).*(H_para1Mat - diag(C(1:end*(1/4)) + ...
    1i*C(end*(1/4)+1:end*(2/4)))*S1_DataMat*diag(C(end*(2/4)+...
    1:end*(3/4))+ 1i*C(end*(3/4)+1:end))))/tempNorm1);

%If necessary, create the output directory
if creatfiles==1
    if ~isfolder(outputDir)
        mkdir(outputDir);
    end
    if ~isfolder([outputDir '/coeffs/'])
        mkdir([outputDir '/coeffs/'])
    end
end

%Use the Matlab canned optimization algorithms.
options = optimoptions('fminunc');
options.MaxFunctionEvaluations = 40000;
options.MaxIterations = 40000;
options.OptimalityTolerance = 0.001;

```

```

%Again, since Matlab optimization only works on real numbers, we have
%to rebuild the Calibration coefficients into the complex number.
CoptNew1_C1 = Copt1(1:numTx) + 1i*Copt1(numTx+1:numTx*2);
CoptNew1_C2 = Copt1(numTx*2+1:numTx*3) + 1i*Copt1(numTx*3+1:end);

%Plot the calibration coefficients found through optimization.
figure
subplot(2,1,1)
plot(abs(CoptNew1_C1))
title(['F = ' num2str(fSim(fx)) 'MHz. Abs Value of Calib. Coeffs C1'])
xlabel('Tx/Rx Path')
legend('Cal. Vals for Imaging Data')
subplot(2,1,2)
plot(angle(CoptNew1_C1))
title('Angle Value of Calibration Coefficients C1')
xlabel('Tx/Rx Path')
legend('Cal. Vals for Imaging Data')

figure
subplot(2,1,1)
plot(abs(CoptNew1_C2))
title(['F = ' num2str(fSim(fx)) 'MHz. Abs Value of Calib. Coeffs C2'])
xlabel('Tx/Rx Path')
legend('Cal. Vals for Imaging Data')
subplot(2,1,2)
plot(angle(CoptNew1_C2))
title('Angle Value of Calibration Coefficients C2')
xlabel('Tx/Rx Path')
legend('Cal. Vals for Imaging Data')

%Using the calibration coefficients found through optimization,
%calculate the calibrated TOTAL fields.
calibratedImageDataMat = diag(CoptNew1_C1)*S1_DataMat*diag(CoptNew1_C2);

%Convert back to a vector format as the CSI code requires the vector
%format.
incount = 1;
calibratedImageDataVec = zeros(numTx*(numRx-1),1);

```

```

calibratedIncidentDataVec = zeros(numTx*(numRx-1),1);
for tx = 1:numTx
    for rx = 1:numRx
        if tx~=rx
            calibratedImageDataVec(incount) = calibratedImageDataMat(tx,rx);
            incount = incount+1;
        end
    end
end

%Plot for calibrated total field vs H_p
figure
subplot(2,1,1)
plot(abs(calibratedImageDataVec));
hold on
plot(abs(H_parallel), 'r-');
legend('Calibrated C1*S1*C1', 'H_parallel');
title('Mag: End of Optimization Comparison: S1/H_parallel');
subplot(2,1,2)
plot(angle(calibratedImageDataVec));
hold on
plot(angle(H_parallel), 'r-');
legend('Calibrated C1*S1*C1', 'H_parallel');
title('Angle: End of Optimization Comparison: S1/H_parallel')

%Compute the Scattered Fields.
%tradedCalScatFieldVec = calibratedImageDataVec - H_parallel;
cc = 1;
newCalScatFieldMat = zeros(numTx,numRx);
newCalScatFieldVec = zeros(numTx*(numRx-1),1);
for tx = 1:numTx
    for rx = 1:numRx
        if tx~=rx
            newCalScatFieldMat(tx,rx) = (1-ignoreMat(tx,rx))*...
                (calibratedImageDataVec(cc)-H_parallel(cc));
            newCalScatFieldVec(cc) = newCalScatFieldMat(tx,rx);
            cc= cc+1;
        end
    end
end

```

```

end
end

%Convert single-shot scattered fields from Hphi to HxHyHz format, and
%write to file to be used as input into CSI.
newScatHxHyHzCalibrated = ...
    convertHPhiToHxHyHz(rxFile,newCalScatFieldVec,numTx,numRx);
outWriteScat = [real(newScatHxHyHzCalibrated)...
    imag(newScatHxHyHzCalibrated)];
dlmwrite([outputDir 'HsctObsCALIBRATED.ONESTEP_2C' num2str(fx)...
    'a1.dat'],outWriteScat,'delimiter','\t');

cc=1;
tradCalScatFieldVec=zeros(numTx*(numRx-1),1);
tradCalCoeffvec=zeros(numTx*(numRx-1),1);
oneshotcalcoeff_l=zeros(numTx,numRx);
oneshotcalcoeff=zeros(numTx*(numRx-1),1);
oneshotScatFieldVec=zeros(numTx*(numRx-1),1);
oneshotTotFieldVec= zeros(numTx*(numRx-1),1);
tradCalTotFieldVec= zeros(numTx*(numRx-1),1);

for tx = 1:numTx
    for rx = 1:numRx
        if tx~=rx
            tradCalCoeffvec(cc) = (1-ignoreMat(tx,rx))*...
                (H_para_incMat(tx,rx)/Sinc_DataMat(tx,rx));
            tradCalTotFieldVec(cc) = (1-ignoreMat(tx,rx))*...
                (tradCalCoeffvec(cc)*S1_Data(cc));
            tradCalScatFieldVec(cc) = (1-ignoreMat(tx,rx))*...
                (tradCalTotFieldVec(cc)-H_para_inc(cc));

            oneshotcalcoeff_l(tx,rx)=CoptNewl_C1(tx)*CoptNewl_C2(rx);
            oneshotcalcoeff(cc)= (1-ignoreMat(tx,rx))*...
                oneshotcalcoeff_l(tx,rx);
            oneshotTotFieldVec(cc)=(1-ignoreMat(tx,rx))*...
                (oneshotcalcoeff(cc)*S1_Data(cc));
            oneshotScatFieldVec(cc)=(1-ignoreMat(tx,rx))*...
                (oneshotTotFieldVec(cc)-H_para_l(cc));
        end
    end
end

```

```

        cc=cc+1;
    end
end
end

%Convert traditional calibrated scattered Fields from Hphi to HxHyHz
%format, and write to file to be used as input into CSI.
tradScatHxHyHzCalibrated = ...
    convertHPhiToHxHyHz(rxFile,tradCalScatFieldVec,numTx,numRx);
outWriteScat = [real(tradScatHxHyHzCalibrated) ...
    imag(tradScatHxHyHzCalibrated)];
dlmwrite([outputDir 'HsctObsCALIBRATED-TRADITIONAL' num2str(fx) ...
    'a1.dat'],outWriteScat,'delimiter','\t');

%Plot, calibration coefficient single-shot vs traditional calibration
figure
subplot(2,1,1)
plot(abs(oneshotcalcoeff))
hold on
plot(abs(tradCalCoeffvec))
title(['Mag Cal Coeff for f = ' num2str(fSim(fx)) ' MHz data']);
legend('Oneshot Cal Coeff','Traditional Cal Coeff',...
    'Per Trasmission Total Field');
xlabel('Channel')
ylabel('Magnitude')

subplot(2,1,2)
plot(angle(oneshotcalcoeff))
hold on
plot(angle(tradCalCoeffvec))
title(['Angle Cal Coeff for f = ' num2str(fSim(fx)) ' MHz data']);
xlabel('Channel')
ylabel('Phase')

%Plot, calibrated scattered fields single-shot vs traditional calibration
figure
subplot(2,1,1)

```

```

plot(abs(newCalScatFieldVec))
hold on
plot(abs(tradCalScatFieldVec))
legend('Oneshot Scattered Field', 'Traditional Scattered Field',...
       'Per Trasmission Total Field')
title(['Mag Scattered Field for f = ' num2str(fSim(fx)) ' MHz data']);
xlabel('Channel')
ylabel('Magnitude')
subplot(2,1,2)
plot(angle(newCalScatFieldVec))
hold on
plot(angle(tradCalScatFieldVec))
title(['Angle Scattered Field Field for f = ' num2str(fSim(fx))...
       ' MHz data']);
xlabel('Channel')
ylabel('Phase')

%Plot, calibrated total fields single-shot vs traditional calibration
figure
subplot(2,1,1)
plot(abs(oneshotTotFieldVec))
hold on
plot(abs(tradCalTotFieldVec))
title(['Mag Cal Total Field for f = ' num2str(fSim(fx)) ' MHz data']);
xlabel('Channel')
ylabel('Magnitude')
legend('Oneshot Total Field', 'Traditional Total Field',...
       'Per Trasmission Total Field');
subplot(2,1,2)
plot(angle(oneshotTotFieldVec))
hold on
plot(angle(tradCalTotFieldVec))
title(['Angle Cal Total Field for f = ' num2str(fSim(fx)) ' MHz data']);
xlabel('Channel')
ylabel('Phase')
end

```

Bibliography

- [1] D. Maier, “Grain operations: Managing stored grain long term,” 2018. [Online]. Available: <http://https://www.world-grain.com/articles/11331-grain-operations-managing-stored-grain-long-term>.
- [2] FAO, “Rural structures in the tropics: Design and development,” 2011. [Online]. Available: <http://www.fao.org/docrep/015/i2433e/i2433e.pdf>.
- [3] W. Muir and N. White, “Grain preservation biosystems,” *Manitoba: Grain Preservation Biosyst.* 1–17, 2000.
- [4] N. White, “Protection of farm-stored grains, oilseeds, and pulses from insects, mites and molds,” *Cereal Research Centre, Agriculture and Agri-Food Canada*, 2000.
- [5] C. Gilmore, M. Asefi, J. Paliwal, and J. LoVetri, “Industrial scale electromagnetic grain bin monitoring,” *Computers and Electronics in Agriculture*, vol. 136, pp. 210–220, 2017.
- [6] N. White and J. Jacobi, “Medical applications of microwave imaging,” *New York: IEEE*, 1986.
- [7] J. Bolomey, A. Izadnegahdar, L. Jofre, C. Pichot, G. Peronnet, and M. Solaimani, “Microwave diffraction tomography for biomedical applications,” *IEEE Trans. Microw. Theory Techn.*, 1986.
- [8] T. M. Grzegorzczuk, P. M. Meaney, P. A. Kaufman, K. D. Paulsen, *et al.*, “Fast 3-d tomographic microwave imaging for breast cancer detection,” *IEEE transactions on medical imaging*, vol. 31, no. 8, pp. 1584–1592, 2012.
- [9] P. Meaney and *et al.*, “Microwave imaging for neoadjuvant chemotherapy monitoring: Initial clinical experience,” *Breast Cancer Res.*, vol. 15, no. 2, p. R35, 1986.

- [10] S. Nelson, *Dielectric properties of agricultural materials and their applications*. Academic Press, 2015.
- [11] S. Nelson and L. Stetson, “Frequency and moisture dependence of the dielectric properties of hard red winter wheat,” *J. Agric. Eng. Res.* 21, 181–192, 1976.
- [12] S. Nelson and et al., “Dielectric properties of agricultural products and some applications,” *Res. Agric. Eng.* 54, 104–112., 1976.
- [13] S. O. Nelson, A. W. Kraszewski, S. Trabelsi, and K. C. Lawrence, “Using cereal grain permittivity for sensing moisture content,” *IEEE transactions on instrumentation and measurement*, vol. 49, no. 3, pp. 470–475, 2000.
- [14] M. Asefi, C. Gilmore, I. Jeffrey, J. LoVetri, and J. Paliwal, “Detection and continuous monitoring of localised high-moisture regions in a full-scale grain storage bin using electromagnetic imaging,” *Biosystems Engineering*, vol. 163, pp. 37–49, 2017.
- [15] W. C. Chew, *Waves and fields in inhomogeneous media*. IEEE press series on electromagnetic wave theory ; 16, New York: IEEE Press, 1999.
- [16] M. Oristaglio and H. Blok, *Wavefield Imaging and Inversion in Electromagnetics and Acoustics*. Cambridge University Press, 2004.
- [17] C. Gilmore, A. Abubakar, W. Hu, T. Habashy, and P. van den Berg, “Microwave biomedical data inversion using the finite-difference contrast source inversion method,” *IEEE transactions on antennas and propagation*, vol. 57, no. 5, pp. 1528–1538, 2009.
- [18] A. Zakaria, I. Jeffrey, J. LoVetri, and A. Zakaria, “Full-vectorial parallel finite-element contrast source inversion method,” *Progress In Electromagnetics Research*, vol. 142, pp. 463–483, 2013.
- [19] P. M. Van Den Berg and R. E. Kleinman, “A contrast source inversion method,” *Inverse problems*, vol. 13, no. 6, p. 1607, 1997.
- [20] R. F. Bloemenkamp, A. Abubakar, and P. M. Van den Berg, “Inversion of experimental multi-frequency data using the contrast source inversion method,” *Inverse problems*, vol. 17, no. 6, pp. 1611–1622, 2001.

- [21] S. Semenov, A. Bulyshev, A. Abubakar, V. Posukh, Y. Sizov, A. Souvorov, P. M. Van den Berg, and T. Williams, "Microwave-tomographic imaging of the high dielectric-contrast objects using different image-reconstruction approaches," *IEEE transactions on microwave theory and techniques*, vol. 53, no. 7, pp. 2284–2294, 2005.
- [22] A. Abubakar, T. M. Habashy, and P. M. Van den Berg, "Nonlinear inversion of multi-frequency microwave fresnel data using the multiplicative regularized contrast source inversion," *Electromagnetic waves (Cambridge, Mass.)*, vol. 62, pp. 193–201, 2006.
- [23] A. Abubakar, P. van den Berg, and J. Mallorqui, "Imaging of biomedical data using a multiplicative regularized contrast source inversion method," *IEEE Transactions on Microwave Theory and Techniques*, vol. 50, no. 7, pp. 1761–1771, 2002.
- [24] A. Abubakar, S. Semenov, V. Posukh, and P. van den Berg, "Application of the multiplicative regularized contrast source inversion method to real biological data," in *IEEE MTT-S International Microwave Symposium Digest, 2005*, pp. 1319–1322, IEEE, 2005.
- [25] C. Gilmore, I. Jeffrey, M. Asefi, N. T. Geddert, K. G. Brown, and J. LoVetri, "Phaseless parametric inversion for system calibration and obtaining prior information," *IEEE Access*, vol. 7, pp. 128735–128745, 2019.
- [26] L. Li, H. Zheng, and F. Li, "Two-dimensional contrast source inversion method with phaseless data: TM case," *IEEE transactions on geoscience and remote sensing*, vol. 47, no. 6, pp. 1719–1736, 2009.
- [27] Z. Hu, L. Lianlin, and L. Fang, "A multi-frequency mrcsi algorithm with phaseless data," *Inverse problems*, vol. 25, no. 6, pp. 065006–, 2009.
- [28] M. Ostadrahimi, P. Mojabi, C. Gilmore, A. Zakaria, S. Noghianian, S. Pistorius, and J. LoVetri, "Analysis of incident field modeling and incident/scattered field calibration techniques in microwave tomography," *IEEE antennas and wireless propagation letters*, vol. 10, pp. 900–903, 2011.

- [29] M. Asefi, G. Faucher, and J. LoVetri, “Surface-current measurements as data for electromagnetic imaging within metallic enclosures,” *IEEE Transactions on Microwave Theory and Techniques*, vol. 64, no. 11, pp. 4039–4047, 2016.
- [30] M. Ostadrahimi, P. Mojabi, C. Gilmore, A. Zakaria, S. Noghianian, S. Pistorius, and J. LoVetri, “Analysis of incident field modeling and incident/scattered field calibration techniques in microwave tomography,” *IEEE Antennas and Wireless Propagation Letters*, vol. 10, pp. 900–903, 2011.
- [31] C. Gilmore, P. Mojabi, A. Zakaria, M. Ostadrahimi, C. Kaye, S. Noghianian, L. Shafai, S. Pistorius, and J. LoVetri, “A wideband microwave tomography system with a novel frequency selection procedure,” *Biomedical Engineering, IEEE Transactions on*, vol. 57, pp. 894–904, april 2010.
- [32] J. A. Tobon Vasquez, R. Scapaticci, G. Turvani, G. Bellizzi, D. O. Rodriguez-Duarte, N. Joachimowicz, B. Duchêne, E. Tedeschi, M. R. Casu, L. Crocco, *et al.*, “A prototype microwave system for 3d brain stroke imaging,” *Sensors*, vol. 20, no. 9, p. 2607, 2020.
- [33] E. Kim, C. T. Mohamadi, M. Asefi, J. LoVetri, I. Jeffrey, and C. Gilmore, “Imaging and calibration of electromagnetic inversion data with a single data set,” *IEEE Open Journal of Antennas and Propagation*, 2021.
- [34] E. Kim, J. LoVetri, I. Jeffrey, and C. Gilmore, “Single data set calibration and imaging with uncooperative electromagnetic inversion systems,” in *2021 15th European Conference on Antennas and Propagation (EuCAP)*, pp. 1–4, IEEE, 2021.
- [35] J. LoVetri, M. A. Asefi, C. Gilmore, and I. Jeffrey, “Innovations in electromagnetic imaging technology: The stored-grain-monitoring case,” *IEEE Antennas and Propagation Magazine*, 2020.
- [36] C. Gilmore, M. Asefi, K. Nemez, J. Paliwal, and J. LoVetri, “Three dimensional radio-frequency electromagnetic imaging of an in-bin grain conditioning process,” *Computers and Electronics in Agriculture*, vol. 167, p. 105059, 2019.
- [37] C. T. Mohamadi, M. Asefi, and C. Gilmore, “Ferrite loaded shielded half loop antenna for electromagnetic imaging inside metallic chambers,” in *2021 19th Interna-*

- tional Symposium on Antenna Technology and Applied Electromagnetics (ANTEM)*, pp. 1–3, IEEE, 2021.
- [38] K. Lawrence, S. Nelson, and P. Bartley Jr, “Measuring dielectric properties of hard redwinter wheat from 1 to 350 mhz with a flow-through coaxial sample holder,” *Transactions of the ASAE*, vol. 41, no. 1, p. 143, 1998.
 - [39] K. Belkebir and M. Saillard, “Testing inversion algorithms against experimental data: inhomogeneous targets,” *Inverse Problems*, vol. 21, pp. S1–S3, 2005.
 - [40] M. Zimmermanns, I. Rolfes, M. Mallach, P. Gebhardt, and T. Musch, “Multiport calibration for microwave tomography systems,” in *2016 German Microwave Conference (GeMiC)*, pp. 96–99, IEEE, 2016.
 - [41] O. Karadima, M. Rahman, I. Sotiriou, N. Ghavami, P. Lu, S. Ahsan, and P. Kosmas, “Experimental validation of microwave tomography with the dbim-twist algorithm for brain stroke detection and classification,” *Sensors*, vol. 20, no. 3, p. 840, 2020.
 - [42] D. O. Rodriguez-Duarte, J. A. Tobon Vasquez, R. Scapaticci, G. Turvani, M. Cavnaro, M. R. Casu, L. Crocco, and F. Vipiana, “Experimental validation of a microwave system for brain stroke 3-d imaging,” *Diagnostics*, vol. 11, no. 7, p. 1232, 2021.
 - [43] M. Hopfer, R. Planas, A. Hamidipour, T. Henriksson, and S. Semenov, “Electromagnetic tomography for detection, differentiation, and monitoring of brain stroke: A virtual data and human head phantom study,” *IEEE Antennas and Propagation Magazine*, vol. 59, no. 5, pp. 86–97, 2017.